Increased water-use efficiency and reduced CO2 uptake by plants during droughts at a continental-scale

Article

Supplemental Material

It is advisable to refer to the publisher's version if you intend to cite from the work. See Guidance on citing.

To link to this article DOI: http://dx.doi.org/10.1038/s41561-018-0212-7

Publisher: Nature Publishing Group

the End User Agreement.

www.reading.ac.uk/centaur

CentAUR

Central Archive at the University of Reading

Reading's research outputs online

Increased water-use efficiency and reduced CO₂ uptake by plants during droughts at a continental-scale

Wouter Peters*[1,2], Ivar R. van der Velde[3,4], Erik van Schaik[1], John B. Miller[4], Philippe Ciais[5], Henrique F. Duarte[6], Ingrid T. van der Laan-Luijkx[1], Michiel K. van der Molen[1], Marko Scholze[7], Kevin Schaefer[8], Pier Luigi Vidale[9], Anne Verhoef[10], David Wårlind[7], Dan Zhu[5], Pieter P. Tans[4], Bruce Vaughn[11], James W.C. White[11]

Supplementary Information

* = corresponding author

1. Environmental Sciences Group, Wageningen University, Wageningen, The Netherlands

2. University of Groningen, Centre for Isotope Research, Groningen, The Netherlands

3. Cooperative Institute for Research in Environmental Sciences, University of Colorado, Boulder, CO, United States

4. Global Monitoring Division, NOAA Earth System Research Laboratory, Boulder, CO, United States

5. Laboratoire des Sciences du Climat et de l'Environnement, LSCE/IPSL, CEA-CNRS-UVSQ, Gif sur Yvette, France

6. Dept. of Atm. Sciences, University of Utah, Salt Lake City, Utah, United States

7. Dept. of Physical Geography and Ecosystem Science, Lund University, Lund, Sweden

8. National Snow and Ice Data Center, University of Colorado, Boulder, CO, United States

9. Dept. of Meteorology, University of Reading, Reading, UK

10. Dept. of Geography, University of Reading, Reading, UK

11. Institute for Arctic and Alpine Research, University of Colorado, Boulder, CO, United States

List of figures and tables:

S1: Definitions of water-use efficiency and relations to discrimination (Δ) and C_i/C_a ratios

Throughout the manuscript, we refer to intrinsic water-use efficiency (iWUE), inherent water-use efficiency (ihWUE), C_i/C_a ratios, Δ-values, and A/g_s. These terms, mainly interchangeably, describe the response of vegetation to drought stress, but from different perspectives. As a generalization, Δ is typically used from an atmospheric (δ_a) or vegetation (δ_v) carbon isotope perspective, iWUE from an ecohydrological perspective, A/g_s from a leaf-exchange perspective, ihWUE from an eddy-covariance observation perspective, and C_i/C_a from a biosphere model perspective. The definitions we followed are described in Farquhar et al (1984), Katul et al.,(2000), Seibt et al., (2008) and Beer et al., (2009):

$$iWUE = \frac{A_n}{g_{s,h_2o}} \approx \frac{g_{s,co_2}(C_i - C_a)}{g_{s,h_2o}} \approx \frac{C_a(1 - C_i/C_a)}{1.6} \qquad \text{(Eq S1)}$$

$$\Delta_{C3} \approx \Delta_d + (\Delta_p - \Delta_d)\left(\frac{C_i}{C_a}\right) \approx (\delta_a - \delta_v) \qquad \text{(Eq S2)}$$

which combine to give:

$$iWUE = \frac{C_a}{1.6}\left(\frac{\Delta_p - \Delta_{C3}}{\Delta_p - \Delta_d}\right) \qquad \text{(Eq S3)}$$

where A_n is the net leaf assimilation rate, C_a and C_i are the CO_2 mole fractions (mol/mol) in the atmosphere and inside the leaf, $g_{s,H2O}$ is the stomatal conductance to water [mol H_2O m^{-2} s^{-1}], Δ_p (27‰) and Δ_d (4.4‰) are the isotopic discriminations during assimilation catalyzed by the enzyme Rubisco in C_3 photosynthesis (p) and molecular diffusion (d) of CO_2 through the stomata, respectively. For inherent water-use efficiency [often reported in gC hPa kg^{-1} H_2O], which can be more readily derived from ecosystem wide eddy-covariance data, we write:

$$ihWUE = \frac{GPP}{g_c} \propto \frac{GPP \cdot VPD}{ET} \qquad \text{(Eq S4)}$$

where g_c is the canopy conductance, derived from the vapor pressure deficit VPD [hPa], and the evapotranspiration ET [kg H_2O m^{-2} s^{-1}] (but we assume soil evaporation ~ 0 as we only use data obtained two days or more after rainfall), and GPP the gross primary production [gC m^{-2} s^{-1}] often derived from net ecosystem exchange (NEE).

Fig S1 shows a set of simulated relations between these variables as derived for a random grid box in Europe for the summer of 2006, to demonstrate that these variables all describe the same response to the

same environmental factors. Obviously, these metrics are always strongly (anti-)correlated which justifies the different viewpoints we present depending on the type of evidence available (observational, numerical, isotope-derived, etc). Note that a recent intercomparison between methods to determine water-use efficiency from measurements showed that the response is not always the same (Medlyn et al., 2017): the scale considered, the plant-functional type, and the C3 or C4 pathway used by plants can have an influence on the relations shown in Fig S1. Our analysis focuses mostly on forested ecosystems and the C3 pathway, which could lead to a small bias compared to gas-exchange measurements when it is based on measurements of the $\delta^{13}C$ isotope in vegetation (δ_v). Atmospheric measurements (δ_a) were not evaluated in that work though.
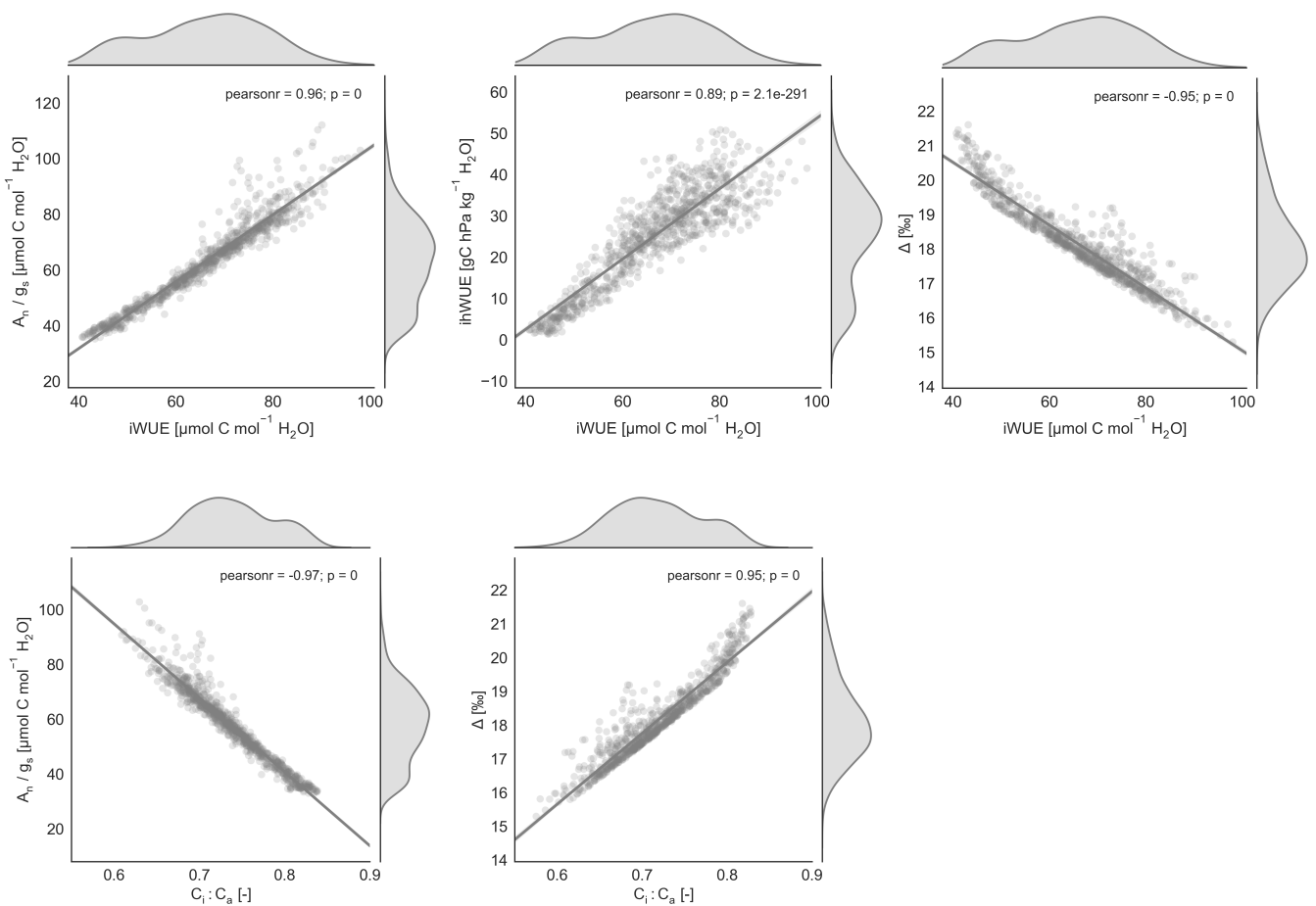
Figure S1: *Relationships between variables used in this study to investigate water-use efficiency. iWUE in these plots is calculated from Eq 2 of the main text as (C_a-C_i)/1.6, Δ comes from the full isotope model in SIBCASA, and C_i/C_a are from SIBCASA too. A random grid box in Europe was chosen for the illustration. Shown are (a) iWUE vs A/g_s ,(b) ihWUE vs iWUE, (c) iWUE vs Δ, (d) C_i/C_a vs A/g_s, and (e) C_i/C_a vs Δ during hours of substantial photosynthetic activity (11am-5pm LT, period 1/6/2006–1/9/2006). The scatter in the C_i:C_a vs Δ in figure (e) is due to the other fractionation terms included in the isolate fractionation model of SIBCASA relative to Eq (S2).*

S2: Observations of CO_2 and $\delta^{13}C$ from the global network

This study uses a large set of CO_2 and $\delta^{13}C$ in CO_2 observations from locations that are visualized in Fig S2. The inversion results presented used 174,000 in-situ CO_2 observations, 24,000 flask measurements of CO_2, and 27,600 $\delta^{13}C$ in CO_2 observations over an 11-year period.
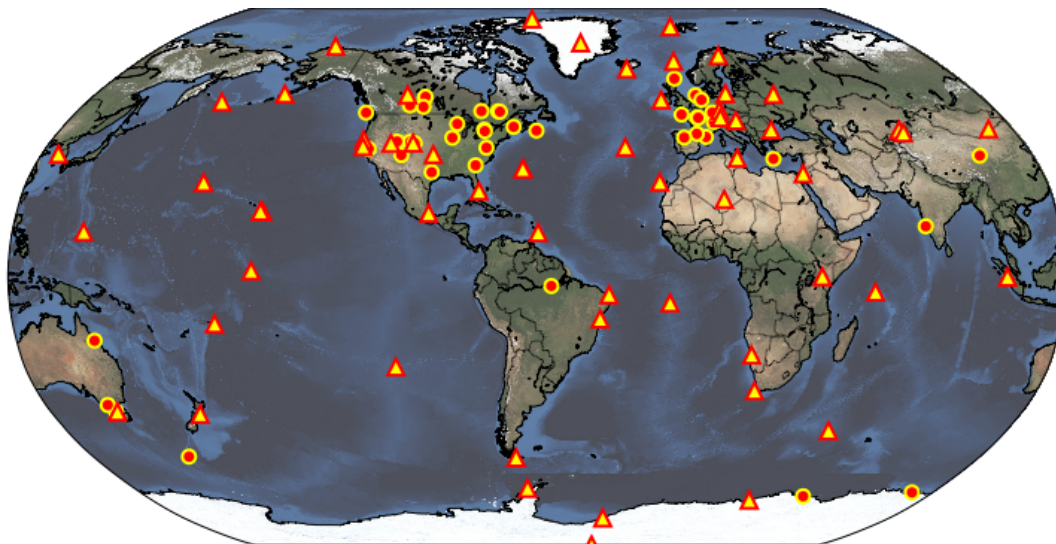
Figure S2: Location of observational sites for this study. Triangles are locations where weekly flasks are filled from the Global Greenhouse Gas Reference Network and analyzed for CO_2 , and subsequently analyzed for $\delta^{13}C$ in CO_2 by INSTAAR (University of Colorado) in Boulder, US. Red circles are locations where daily in-situ measurements of CO_2 are available.

The temporal coverage of the available observations (not shown) is excellent (typically 1x 7 days or more) and we verified that no major data gaps or asymmetries in coverage exist, which makes it unlikely that our results are influenced by uneven coverage of the available observations. More observations of $\delta^{13}C$ are available from several programs, including those of Environment Canada, Scripps Institute for Oceanography, and several European laboratories. We did not use these in the present study to perform the inversions. Mostly, these measurements are already part of ongoing intercomparisons and are calibrated to the same scale, such that they could serve as additional constraints on spatiotemporal patterns of isotopic discrimination (Δ) in follow-up studies. Compared to the atmospheric CO_2 and $\delta^{13}C$ gradients we aim to interpret, the measurement precision of CO_2 is very high (<0.1 ppm for typical gradients of 1-10 ppm) while that of $\delta^{13}C$ is lower (<0.03‰ for gradients of 0.05-0.5‰).

We illustrate the match to such observations with three well-known sites in the Northern Hemisphere: Mauna Loa, Barrow, and Mace Head. Fig S3 show the match of the inversion after optimizing only the NEE using CO_2 mixing ratios (step 1 from the two-step inversion) and after optimizing NEE and Δ simultaneously using CO_2 and $\delta^{13}C$ (from the new-CO2C13 inversion). The PDFs of the residuals are

shown on the right-hand-side, including the standard deviation and RMSD. They show that at all three sites, the bias was already small compared to measurement precision of $\delta^{13}C$ after the CO_2-only inversion but the standard deviation of the residuals (almost equal to RMSD) reduces further due to the use of the
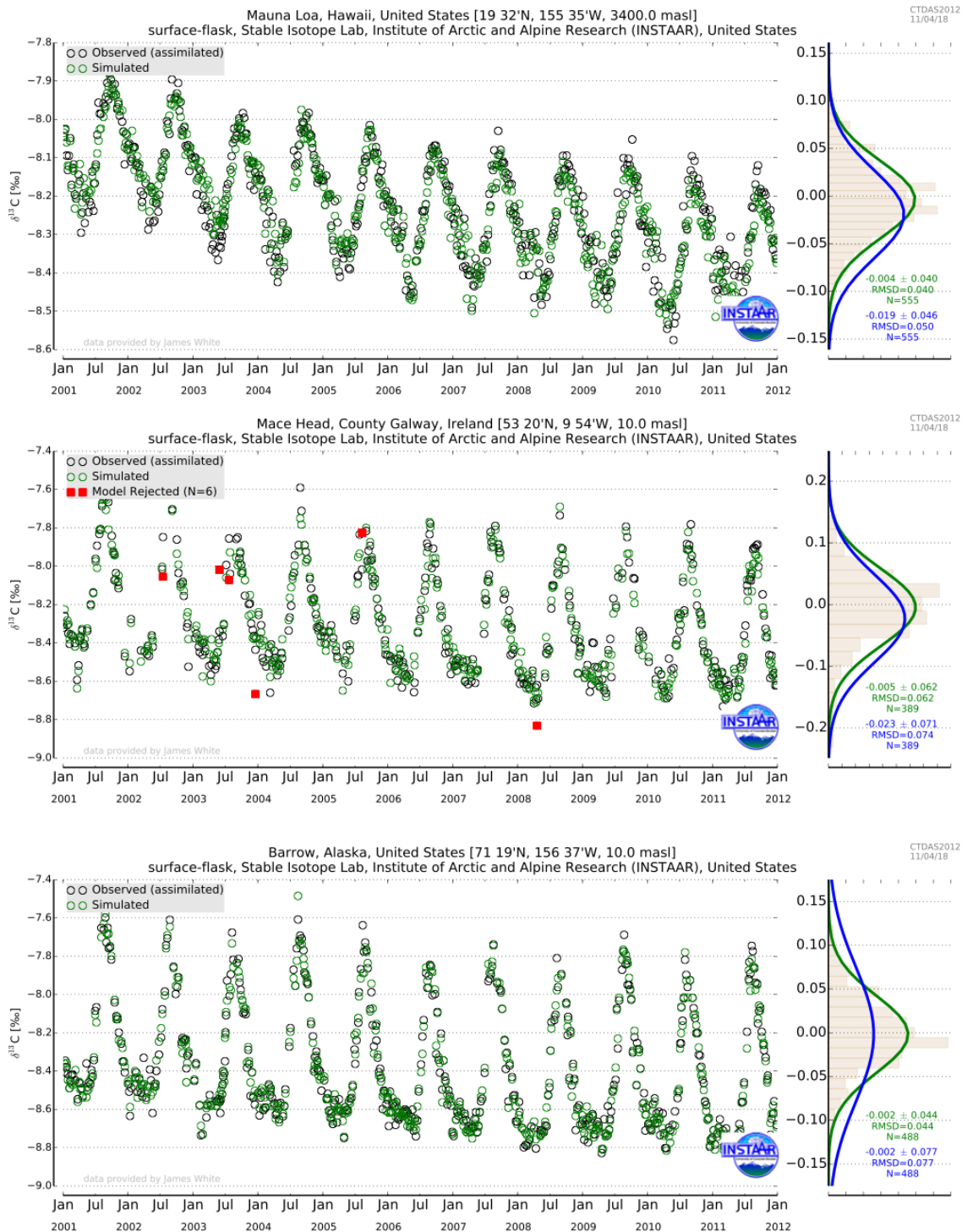
Figure S3: Observed (black) and simulated (green) $\delta^{13}C$ in CO_2 ratios for three sites in the NH: Mauna Loa, Mace Head, and Barrow. Rejected simulated values are highlighted in red (>3 times MDM). The distribution of residuals is provided on the right-hand-side, showing unbiased residuals after the CO_2-only inversion, and a reduction in the residual spread (and hence lowering of the RMSD) when also using $\delta^{13}C$ observations to optimize Δ-values.

δ¹³C observations. This agrees with our suggestion that the inversion mostly uses δ¹³C to capture a fraction of variability that is not readily resolved from CO_2-alone, or not attributable to NEE because of the CO_2 constraint. Changes are relatively small on an absolute δ¹³C-scale (~0.01‰, 0.012‰, 0.033‰ RMSD at Mauna Loa, Mace Head, and Barrow respectively) when compared to the single measurement precision on a flask pair (0.02‰), but the large number of observations per site (555, 389, 488) nevertheless make this a relevant reduction in residuals. We furthermore stress that this improvement is quite systematic across the NH, as seen in Fig 7a of van der Velde et al., (2018). It shows the fraction of the RMSDs for all sites. On the NH, N=19 sites show a >5% improvement, N=13 sites stay within the 5% margin, and N=0 sites deteriorate >5% in RMSD.

We simulate in van der Velde et al, (2017) the following mass-balance equation for δ¹³C in CO_2 (Tans et al., 1993):

$$CO_2 \cdot \frac{d\delta_{13}}{dt} = F_{ff} \cdot (\delta_{ff} - \delta_a) + F_{fire} \cdot (\delta_{bio} - \delta_a) - \\ N_{bio}\Delta_{bio} - N_{oce}\Delta_{ocean} + \\ D_{bio} + D_{oce}$$

$$(Eq \ S5)$$

where δ¹³C is the isotope ratio of ¹³C/¹²C, F refers to fluxes from fires and fossil fuels (ff), while N is the net carbon flux from the ocean, and biosphere (NEE). D refers to the disequilibrium fluxes, δ_{bio} and δ_{ff} are the signatures of burning sources, while the terrestrial and oceanic discrimination are labeled with Δ.

We note that terrestrial discrimination (Δ) in our model only refers to photosynthetic discrimination, and not to post-photosynthetic changes in isotope ratios which are known to occur (see for example Brüggemann et al., 2011 and references therein, as well as Ekblad and Hogberg, 2001). As far as we know there is currently no known biophysical formula to capture this discrimination across gradients of vegetation types, and environmental conditions similar to the well-known and highly reproducible Farquhar equation for photosynthesis discrimination. To make an impact on our analysis, post photosynthetic discrimination needs to exhibit two properties: (1) is that it varies from year-to-year with environmental conditions, and (2) that the signals are carried into the atmosphere by a large enough respiration flux to make an impact on δ¹³C in CO_2 across the northern hemisphere.

For (1), we note that most observations so far show differences in δ¹³C composition between structural pools in a plant which require post-photosynthetic discrimination to have occurred, but it is not clear to which degree the processes responsible actually change over time. Some exhibit diurnal cycles, but measurements and experiments on seasonal and longer time scales are still lacking. We furthermore note that if this discrimination happens inside pools with a relatively slow turn-over time (i.e., these are typically the larger pools like stems and soils), they are unlikely to contribute strongly to variations in the atmospheric flux, as respiration will carry the average signature of the whole pool which is unlikely to vary quickly for large pools. So the best way to satisfy (1) is if a discrimination process would happen at the moment of conversion of plant biomass to atmospheric CO_2 and it is not simply constant, but is a function of an environmental condition with substantial year-to-year changes (such as temperature, or soil moisture, or water content of the biomass). This is most likely to occur for pools of surface litter, and soil organic matter that is most easily mobilized and we note that these are associated with a relatively small fraction of
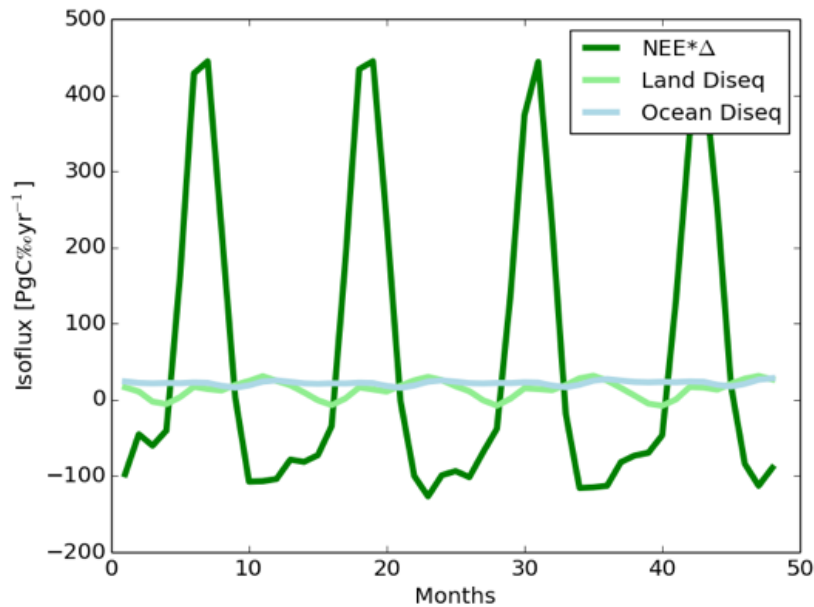
Figure S4: The magnitude of isofluxes from various term in the $\delta^{13}C$ budget.

the total respiration flux to the atmosphere. To satisfy (2), this in turn means that very large variations in discrimination are needed to create sufficient leverage on the atmosphere. Until further research as outlined in the work of Brüggemann et al., (2011) is available, we can not quantify the impact of such variations on our simulated Δ values. We note though that in the work of Ekblad and Hogberg (2001), a lengthy discussion on this topic ends with the conclusion that "… a growing body of results suggests that 13C-discrimination during respiration is negligible.".

When we simulate the atmospheric mole fractions and isotope ratios at the locations in Fig S2, the distributions of $\delta^{13}C$ and CO_2 residuals (simulated minus observed) are already small. Partly, this results from the scaling of the isotopic fluxes specifically to balance the decadal $\delta^{13}C$ budget in the presence of uncertain disequilibrium fluxes D_{bio} and D_{ocean}. These disequilibrium fluxes present the return of carbon from oceanic and terrestrial reservoirs (see van der Velde et al., 2017 and Alden et al., 2010 and Eq S5) with enough delay to be different from today's atmospheric isotope ratios, due to the ongoing addition of isotopically light fossil-derived CO_2 (the so-called Suess effect (Suess, 1962)). In addition to these disequilibrium fluxes, the use of the SIBCASA biosphere model and other fluxes as in van der Velde et al., (2013, 2017) captures a large fraction of the synoptic and seasonal variability that are typically stronger than the interannual variability in $\delta^{13}C$ mole fractions.

Without this decadal balancing through the disequilibrium fluxes, trends in simulated-minus-observed $\delta^{13}C$ residuals would wrongly be aliased into trends in the estimated Δ_{bio} and fluxes from the data assimilation system, as presented in Fig 1 of the main text. Removing this residual trend before our analysis prevents

this, but also means that we cannot diagnose multi-decadal trends in Δ from the available observations as done for instance in the recent work of Keeling et al. (2017). Furthermore, to extend our analyses to more than 11 years would require a more sophisticated method to incorporate the disequilibrium fluxes before the inversion. Hence we limit ourselves here to the 2001-2011 period, and to the interannual variability of Δ.

Interannual variability in the ocean disequilibrium fluxes could also play a role in explaining the atmospheric $\delta^{13}C$ signal, but we think it is unlikely to have been a factor in the analysis of the summertime anomalies presented in the main text. This is based partly on Fig S4, showing the much larger isofluxes from terrestrial net exchange than from the ocean or land in summertime. We furthermore note that according to the fluxes calculated by Rödenbeck et al., (2013) the IAV of gross ocean fluxes on the NH is surprisingly small. This is shown in Fig S5 which documents the flux anomalies (i.e., relative to the subtracted mean) of the net and gross ocean CO_2 fluxes since 1985 (until present-day). It shows that on a decadal time scale, variations in ocean-atmosphere flux (Foa) in the NH Atlantic and Pacific ocean are typically <1.0 PgC/yr peak-to-trough, suggesting a 1-σ of less than 0.3 PgC/yr. This is confirmed when integrating gross ocean-atmosphere fluxes from Rödenbeck et al., (2013) over the NH, shown in Table S1. IAV is between ±0.28 and ±0.59 PgC/yr depending on the chosen size of the NH ocean basins included.

Contributions to the IAV that are considered in these fluxes are (a) variations in pCO2 of the ocean based on the SOCATv1.5 underway pCO2 measurements which typically have good coverage of these regions, (b) variations in the ocean-atmosphere exchange coefficient k dependent on temperature and solubility, and
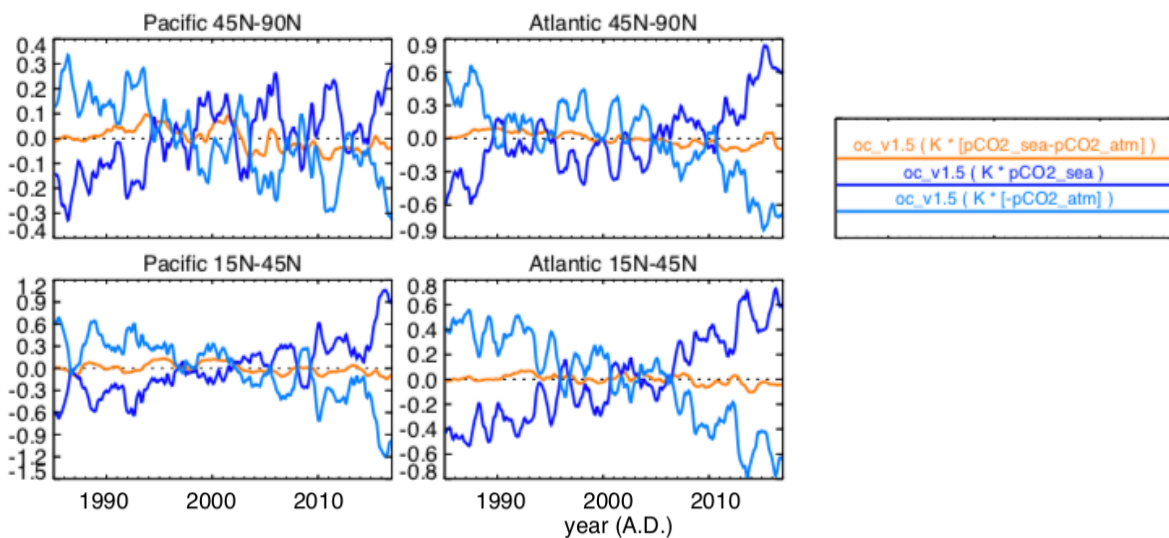
Figure S5: Anomalies relative to the long-term mean in the gross sea-air ocean fluxes from Rödenbeck et al., (2013), for four major ocean basins in the NH. Decadal variations are larger than interannual variations, and gross flux variability exceeds the net flux variability. The calculated IAV includes contributions from changes in surface ocean pCO2, wind speed, and solubility. When integrated over the period 2000-2012, the total gross flux for the NH oceans (>30N) is 14.5±0.28 PgC/yr.

(c) changes in wind speed. In the calculation of the gross ocean flux the largest term by far is the pCO2 value itself, which varies by just a few percent. And although gross ocean flux variability is indeed larger than the IAV on the net ocean flux (yellow color in same plot), it would not be sufficient at all to drive a large variability in ocean disequilibrium isoflux (Foa*(δoa-δao)), unless very large changes in the isotopic signatures of the exchange occurred.

	>30N	>0N	Global
Fnet	-1.01 ± 0.12	-0.99 ± 0.16	-1.91 ± 0.35
Foa	+14.48 ± 0.28	28.99 ± 0.59	+86.81 ± 2.56
Fao	-15.49 ± 0.38	-29.98 ± 0.68	-88.72±2.73

Table S1: Carbon fluxes into (Fao) an out of (Foa) the ocean, and their sum (Fnet). Fluxes are summed over the globe, the NH, or the HN north of 30N and averaged over 12 years (2000-2012). The 1-σ standard deviation is given as well, which shows the interannual variability. Units are PgC/yr

In (δoa-δao) the effect of changing ocean fractionation can play a role. In our inversion we used two different sets of input data to make (1) the ocean net fluxes (extrapolation of Jacobsen et al., (2007) fluxes) and (2) the ocean disequilibrium fluxes. In (1) we used a constant fractionation factor for atmosphere-ocean exchange (ϵao), realizing that this term will only be relevant for the mean δ¹³C budget and not its variance. For (2) we did include interannually varying SST, and its effect on ϵoa (Zhang et al., 1995) as well as on ocean-atmosphere exchange coefficient (k). This was in addition to interannually varying wind speeds. This choice acknowledged that all of these vary enough to possibly matter given the large gross flux they are multiplied with. What we did not include was interannually varying δ¹³C of DIC in the surface ocean, for a lack of measurements. Note that this is also true for pCO2 in our inversion, but the fluxes from Rödenbeck above, that were calculated with varying pCO2 included, suggest a considerable variability due to pCO2 changes, at least on the NH.

When we next look at literature on variations of δ¹³C of DIC, we note that it was measured repeatedly between 1995 and 2014 in the North Atlantic (most of these cruises took place in summer months). The data show very little variability between cruises in different years (Becker et al., 2016, ESSD, see their Fig 5), and certainly not of the magnitude of ±0.5 ‰ IAV as needed in our analysis. Larger signals are the slowly changing δ¹³C of the surface ocean (Suess effect) and a large seasonal cycle in δ¹³C in DIC (~0.7‰

peak-to-trough) which we indeed capture in the $\delta^{13}C$ of our disequilibrium fluxes at for example the Atlantic BATS station and the Pacific HOT station.

This seasonal cycle is set by summer accumulation of atmospheric CO_2 (representing the current atmospheric $\delta^{13}C$ signature) in the more stably stratified mixed-layer, and this atmospheric imprint during summer is subsequently "reset" in winter when older water from the deeper ocean is mixed upward. Given the size of this DIC input from below in the NH we do not expect any influence of the previous summer's atmospheric signature to persist beyond this period of a few months. The $\delta^{13}C$ of the upwelling water in winter, coming from such a large ocean reservoir, are unlikely to change strongly from year to year beyond the longer-term Suess-effect. In other words, the ocean gets reset to nearly the same winter values each year, and then changed mostly by the input of atmospheric $\delta^{13}C$ which does not force a disequilibrium.

Most importantly, in the consideration of variability in isotopic signatures it means that especially the summer ocean fluxes contribute least to the disequilibrium since the DIC is more strongly influenced by input of very recent atmospheric CO_2. This is confirmed by modeling studies such as by Tagliabue et al., (2008) which find that "on interannual timescales, although the variability in $\delta^{13}C$ in DIC is a first order function of the atmospheric $\delta^{13}C$ in CO_2 and overall carbon flux, the spatial distributions are controlled by the degree to which surface waters are exposed to the atmosphere." The latter part of this statement refers to the global pattern of oceanic uptake and release of CO_2.

S4: Robustness of the Northern Hemisphere anomalies in Δ and NEE

The reported high correlation and slope between net carbon uptake and Δ in Fig 1 of the main text is robust and significant. We performed a set of four alternative inversions to optimize Δ and NEE to test the robustness of this signal against the setup of the inversion system used to derive them. The result in Fig 1 of the main text uses the base inversion (B1) with the other results shown in Table S2 and Fig S6.

Three inversions were nonlinear (B1, T1, E1), because Δ and NEE were scaled simultaneously, even though they are multiplicative factors in the budget equation of $\delta^{13}C$ (Eq S5). Inversion B1 was our base case setup. Inversion T1 used the convection fields from ECMWF ERA interim meteorological fields rather than the default TM5 convection scheme. Inversion E1 used different model errors on the $\delta^{13}C$ observations. The linear inversion (L1) had the same setup as our baseline inversion but the optimization proceeds in two steps: we first optimized NEE based on CO_2 observations only, and then we use $\delta^{13}C$ to optimize Δ in a subsequent inversion with NEE (and its uncertainty) from step 1. All four inversions show a significant correlation between NEE and Δ. This correlation does not originate from our SIBCASA terrestrial biosphere model (see Section S5), nor does it emerge from more traditional inverse estimates either based on atmospheric CO_2 observations alone (C1), or from both CO_2 and $\delta^{13}C$ observations that constrain only NEE (C2).
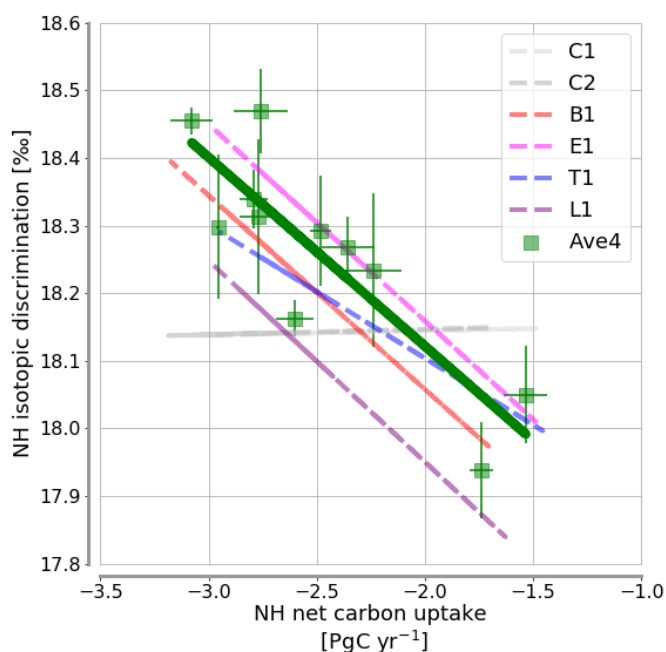
Figure S6: Annual mean net carbon uptake versus isotopic discrimination (Δ) integrated over temperate and boreal Northern Hemisphere land areas (green squares and fitted slope). Individual results from the optimization of NEE with atmospheric CO_2 observations (orange line, underneath the yellow line), from the optimization of NEE with atmospheric CO_2 and $\delta^{13}C$ observations (yellow line) and from four different optimizations of NEE and Δ with atmospheric CO_2 and $\delta^{13}C$ observations (described in Table S2). Statistics of the linear regression are included in Table S2.

Table S2: *Statistics for the NEE-Δ relation over the NH land areas from a set of different estimates. For easier comparison with other inverse modeling results we based this comparison on TransCom region definitions (NH land = TC1 + TC2 + TC7 + TC8 + TC11), and therefore statistics of the base run are slightly different from the main text. Slopes that are significantly different from 0 (p<0.05, N=9) are highlighted in bold. Note that C1 and C2 are not used in the average, since these inversions did not optimize Δ. Simulation T1 lost significance when detrending NEE and Δ because its record is based on the period 2001-2008 only, due to technical limitations.*

	Ave	B1	T1	E1	L1	C1	C2
	Characteristics of model formulation						
characteristic	average of 4 inversions {B1,L1,E1,T1}	base	alternative convection	larger δ¹³C errors	linear inversion	CO₂-only	NEE-only
color in Fig S3	green, with symbols	red	blue	magenta	purple	light grey	dark grey
	2001-2011 Δ-NEE relationship over NH land areas (boreal + temperate), including trend						
correlation [-]	-0.86	-0.79	-0.70	-0.78	-0.79	+0.14	+0.18
slope [‰/(PgC/yr)]	-0.28	-0.29	-0.20	-0.29	-0.30	+0.01	+0.08
p-value [-]	**0.0007**	**0.003**	**0.05**	**0.004**	**0.02**	0.69	0.59
IAV in Δ [‰ 1σ]	-	±0.17	±0.14	±0.17	±0.18	±0.02	±0.02
IAV in NEE [PgC/yr, 1σ]	-	±0.46	±0.49	±0.46	±0.47	±0.46	±0.49
	2001-2011 Δ-NEE relationship over NH land areas (boreal + temperate), trend removed						
correlation [-]	-0.74	-0.65	-0.41	-0.65	-0.71	+0.29	+0.46
slope [‰/(PgC/yr)]	-0.22	-0.24	-0.13	-0.24	-0.34	+0.02	+0.03
p-value [-]	**0.009**	**0.03**	0.312	**0.03**	**0.05**	0.283	0.159
IAV in Δ [‰ 1σ]	-	±0.13	±0.13	±0.15	±0.18	±0.02	±0.02
IAV in NEE [PgC/yr, 1σ]	-	±0.36	±0.33	±0.32	±0.36	±0.36	±0.35

The range of values we observe in Fig S3 is not unexpected for NEE, and is caused in part by the increase in biospheric uptake reported previously for the Northern Hemisphere (Graven et al., 2013; Le Quere et al., 2015), also visible in Fig 1. It is however less clear whether Δ should similarly increase over time. Higher NEE values would automatically lead to higher isofluxes of δ¹³C towards the atmosphere and it does not necessarily require the Δ-values to increase too. Nevertheless, recent research has shown the likely influence of CO_2 increases on Δ and on $δ_a$ in long-term records through photorespiration (Keeling et al., 2017). From the full Farquhar (1983) equation for isotopic discrimination we estimate this effect to have

been small over the decade we simulated, which we later confirmed with a separate simulation that included the photorespiratory impact on Δ (data not shown).

With observed trends in CO_2 and $\delta^{13}C$ abundances, and possible trends in Δ and in NEE over a decade, it is important to consider the possibility that correlations for both inversely derived and from biosphere model derived Δ and NEE are partially related to their corresponding trends rather than IAV. We performed a linear detrending of the 11-year NEE and Δ time series for the Northern Hemisphere, to test this possibility for our inversion. As shown in Table S2, even after detrending the correlation between NEE and Δ remains large and statistically significant as in Fig 1 of the main text. This provides further evidence that droughts and stomatal conductance change in concert over these large scales, and that the scaling of the disequilibrium fluxes described in paragraph S1 effectively prevented a trend in Δ to be derived. We note that the possible propagation of changes in Δ into this disequilibrium flux itself which we do not consider in the inversions was specifically tested as part of the methodology described in van der Velde et al., (2017), and could reduce the required IAV in Δ derived in Fig 3 and Table S3 by a maximum of 10% only.

For the biosphere models considered, the influence of detrending is larger because NEE and Δ result from their internal carbon balances, which are not necessarily in steady-state over a decade. For example, the SIBCASA model, when detrended, shows a correlation (-0.51) between NEE and Δ that previously remained hidden inside the trend and very small IAV of Δ. Just like for the other models, these slopes remain statistically not different from zero and both NEE-Δ correlations and IAV in Δ are still very small after detrending.

S5: Inherent WUE determined from eddy-covariance sites

Measurements from eddy-covariance sites in Europe and North America (Fluxnet and Ameriflux) confirmed that inherent water use efficiency (see Eq S4) increased during severe droughts. Table S3 presents the change in annual mean canopy conductance, gross primary production, and water-use efficiency during the 2003, 2006, and 2010 droughts across ten forested sites that experienced low SPEI conditions. The European drought of 2003 caused 13-48% lower conductance along with 8-48% reduced GPP across all nine sites analyzed across the Netherlands, Germany, France, Belgium, and Italy. Similar effects can be observed on canopy conductance at three sites where SPEI was below -1.0 during the European drought of 2006, and at one available site during the 2010 Russian drought. At nine out of thirteen sites in Table S3 the reduced GPP and canopy conductance led to significantly increased ecosystem water-use efficiency indicative of reduced C_i/C_a and hence Δ. Although different methods to determine WUE were shown to not always yield the same results (Beer et al., 2009) their correspondence reinforces the complementarity of our large-scale diagnosis with those available at local scales.

The analysis of eddy-covariance data in Table S3 is based on half-hourly averaged values between April and September reported in the FLUXNET fair use database and in Kurbatova et al., (2013). We excluded days with precipitation and the two consecutive dry days after rainfall to capture only the leaf transpiration rather than the soil evaporation in the measured total evapotranspiration. We show inherent WUE, specifically suitable to evaluate WUE at the ecosystem scale from eddy-covariance measurements. Daily averages were calculated and filtered for unrealistic negative nighttime fluxes and low turbulent conditions.

Due to lack of direct isotope and Δ measurements, ihWUE is the only widely available metric to investigate changes in canopy conductance. During severe droughts the VPD is generally high and leaf stomata will close, resulting in a smaller stomatal conductance value and a larger VPD/ET ratio. Subsequently, this leads to increases in the CO_2 gradient between atmosphere and leaf interior, a larger ihWUE and a smaller leaf level Δ value as predicted by Eq S1-S3. We specifically use inherent WUE because it is more informative in describing biochemical functions in plants than the more general GPP/ET relationship used for WUE at the ecosystem level (Beer et al., 2009). Fig S1 demonstrates the relationship between ihWUE and iWUE in our SIBCASA model, confirming their high similarity.

Table S3: Analysis of growing season (Apr-Sep) mean water-use efficiency (see S1), canopy conductance, gross primary production, for the severe drought year (t) and the surrounding non-drought years (t-1, t+1) for a selection of eddy-covariance sites. The last column gives the GPP-weighted mean SPEI index during the drought year at the site location. Canopy conductance calculations are based on inverting the Penman-Monteith equation using the measured latent heat flux and net irradiance and an estimate of the ground heat flux. Green indicates a change in WUE, canopy

conductance, GPP, or SPEI that agrees with the newly derived large-scale response to a severe drought, and red vice versa.

Country	Site name	Site ID	ihWUE ± std err	ihWUE ± std err	Canopy conductance	Canopy conductance	change in GPP	SPEI
			drought	non-drought	drought	non-drought	difference	drought
			[g C hPa/ kg H_2O]	[g C hPa/kg H_2O]	[mol/ m^2/s]	[mol/ m^2/s]	[g C/m^2/ month]	[-]
Europe 2003 drought (April - September)								
Belgium	Viesalm	BE-Vie	41.2±4.5	21.2±3.8	0.31	0.42	-8.4	-1.2
France	Hesse Forest	FR-Hes	37.3±3.8	38.4±3.4	0.26	0.30	-10.0	-1.6
France	Puechebon	FR-Pue	38.0±6.1	27.7±2.4	0.24	0.32	-29.2	-2.0
Germany	Hainich	DE-Hai	56.8±5.1	56.3±2.8	0.29	0.39	-22.4	-1.5
Italy	Castelporziano	IT-Cpz	29.5±7.8	22.6±4.6	0.28	0.37	-31.0	-1.5
Italy	Roccarespampani	IT-Ro1	41.6±1.9	31.1±1.7	0.32	0.42	-48.2	-1.5
Italy	San Rossore	IT-SRo	21.3±5.0	12.2±1.7	0.23	0.44	-23.0	-2.0
Netherlands	Loobos	NL-Loo	34.3±7.9	31.1±4.0	0.33	0.39	-12.7	-1.2
Spain	El Saler	ES-Es1	9.6±2.3	14.9±1.0	0.48	0.55	-38.2	-1.1
Europe 2006 drought (April - September)								
France	Puechebon	FR-Pue	35.8±3.8	36.3±2.8	0.17	0.24	-47.7	-1.3
Netherlands	Loobos	NL-Loo	69.3±6.8	38.9±5.9	0.38	0.47	-32.7	-1.3
Spain	El Saler	ES-Es1	16.0±1.2	12.7±0.9	0.45	0.51	-18.7	-1.1
Russia 2010 drought (April - September)								
Russia	Tver Oblast	Ru-Fyo	31.3±2.8	18.3±1.0	n/a	n/a	-41.8	-1.5

For our site-specific analysis of ihWUE we used daily GPP, ET, VPD and canopy conductance from the Fluxnet free fair use database. We excluded the days with precipitation and the two consecutive dry days after rainfall to capture only the leaf transpiration rather than the soil evaporation and interception in the measured total evapotranspiration (Beer et al., 2009). More recent half-hourly data from Ru-Fyo (Tver, Russia) came from Kurbatova et al. (2008, 2013). Daily averages were calculated and filtered for unrealistic negative nighttime fluxes during low turbulent conditions.

During the European droughts of 2003 and 2006 we found considerable increases in ihWUE in comparison to the neighboring (wetter) years for a selection of sites. This behavior was not confined within a small

region or country, but was measured across Europe. Together with the reduction in canopy conductance it confirms the large extent of the drought event as is indicated by the SPEI index. For three of these sites we plotted (Fig S7) the relationship GPP*VPD vs ET: Viesalm, Belgium (BE-Vie), Roccarespampani, Italy (IT-Ro1) and Loobos, Netherlands (NL-Loo). All three sites experienced reductions in GPP in the drought year. In addition, canopy conductance was more than 18% lower, and the slopes of the linear regression lines showed an increase during the drought year. All these findings point towards a continental wide reduction in Δ in 2003 and 2006.

For the United States, in 2002, we found similar increases in ihWUE in California (US-Ton), Indiana (US-MMS) and Maine (US-Ho1). However, for most of the other available sites there was no clear drought signal present in 2002. Some of the available US sites contained irrigated crops that would be protected from severe drought conditions. In addition, most of the sites were located outside the SPEI drought region, which made it difficult to assess the drought response in a similar way as in Europe.
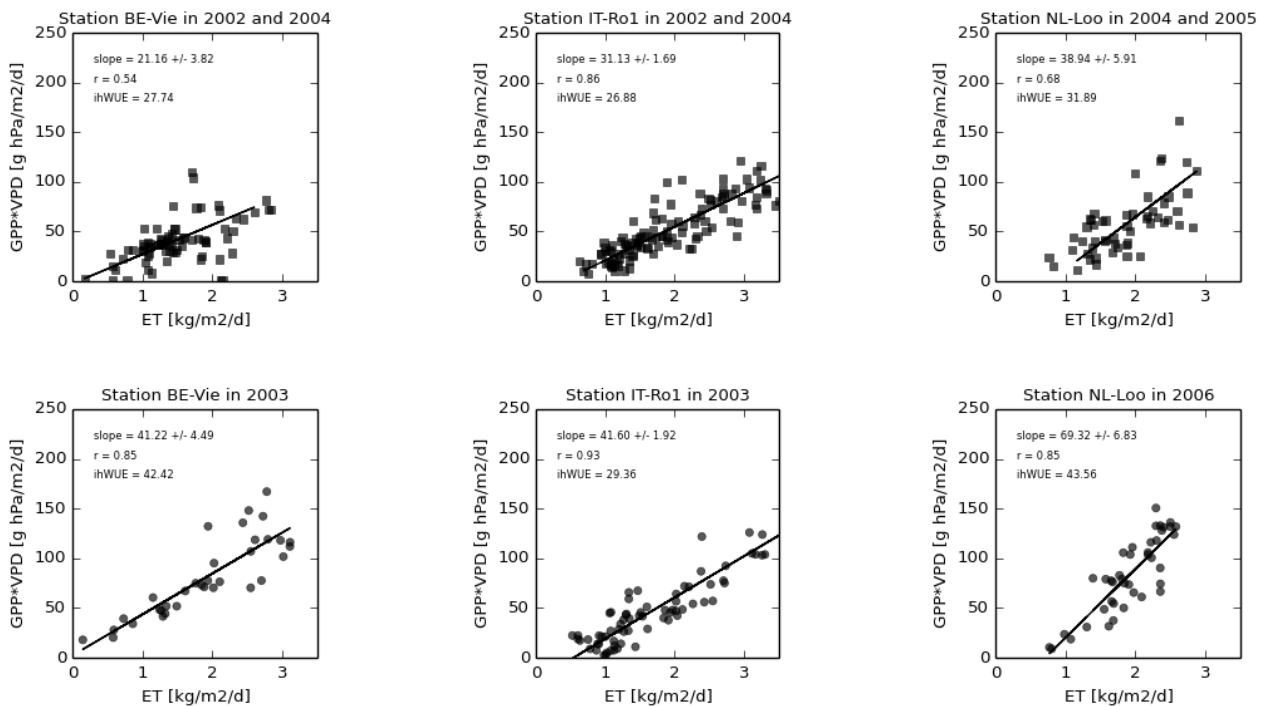
Figure S7: *Relationship between daily mean GPP*VPD and ET measured for Vielsalm, Belgium (first column), Roccarespampani, Italy (second column), and Loobos, Netherlands (third column). Top panels shows the data from 2 relatively wet years and bottom panels show the data from the drought year. Slope and correlation coefficient r are determined by linear regression. ihWUE is derived from the annual sums of GPP*VPD and ET.*

S6: Biosphere model drought formulations

We have included a brief description of each of the 6 biosphere models used in our study below, with a focus on the formulation of their drought response. For convenience, we have summarized their most important differences in Table S4, repeated from the Online Methods, below. Where possible, we have characterized each model's soil moisture drought response with a code (C1,…C6) which corresponds to the responses (but not necessarily the exact formulations) of the different coupling methods presented in the work of Egea et al. (2011). These authors demonstrated that only configurations C1, C5, and C6 capture the observed increase in intrinsic water-use efficiency towards higher soil moisture stress. We refer to the original paper of Egea et al. for more details.

Table S4: Overview of the drought response formulations used in the suite of land-surface models represented in Fig 3 of the main text. Abbreviations used: RH is Relative Humidity, ET is evapotranspiration, VPD is vapor pressure deficit, g_s is stomatal conductance, g_m is mesophyll conductance, V_{max} is the maximum carboxylation capacity, J_{max} is the maximum electron transport rate, and β is the model specific soil moisture stress factor ranging from 0 to 1.0.

Model Name	SIBCASA	LPJ-GUESS	JULES	CLM-C13	ORCHIDEE	LPJ-C13
Weather forcing	ECMWF ERA-Interim	CRU TS v.3.22 & CRU-NCEP v7	CRU-NCEP	CRU-NCEP	CRU-NCEP	CRU TS v.3.22
Leaf-level drought stress response						
Response g_s	yes, to RH	yes, to ET	yes, to VPD	yes, to RH	yes, to VPD	yes, to ET
Response g_m	none	none	none	none	none	none
Response V_{max}	none	none	none	none	none	yes
Response other	none	none	g_s to O_3	none	none	none
Photosynthesis model	Farquhar-Collatz	Farquhar-Collatz	Farquhar-Collatz	Farquhar-Collatz	Farquhar-Collatz	Farquhar-Collatz
Conductance model	Ball-Berry	Prentice, Haxeltine	Jacobs	Ball-Berry	Yin and Struik	Prentice, Haxeltine
Root-zone drought stress response						
Response g_s	none	yes, to C_i/C_a	none	yes, to β	yes, to β	yes, to C_i/C_a
Response g_m	yes, to β	none	none	none	yes, to β	none
Response V_{max}, J_{max}	yes, to β	none	yes, to β	yes, to β	yes, to β	none
Response respiration	yes, to β	none	yes, to β	yes, to β	yes, only R_d	none
Response other	none	C_i/C_a to β	none	none	none	C_i/C_a to β
WUE response type	C4	C1	C2	C5	C6	C1

SIBCASA

In SIBCASA the Farquhar assimilation formulations (Farquhar et al., 1980) in combination with three different resistances placed in series predict the CO_2 flux from the leaf boundary (r_b), through the stomatal openings (r_s), and dissolution in mesophyll (r_m). From the SiB model (Sellers et al., 1996) SIBCASA adopted the Ball-Berry formulation for stomatal conductance ($g_s = 1/r_s$):

$$g_s = m \frac{A_n}{C_s} h_s P + b \qquad \text{(Eq S6)}$$

where A_n is the net assimilation rate (assimilation minus leaf respiration), C_s is CO_2 partial pressure at the leaf surface, P is the atmospheric pressure, and h_s is the RH at the leaf surface. The slope and intercept parameters m and b are empirically determined from observations (in SIBCASA: C3 plants: m=9, C4 plants m=4). Closing of the stomata (e.g. due to low RH) lowers the stomatal conductance and the ratio between CO_2 in stomatal cavity and atmosphere (C_i/C_a). This in turn lowers the Δ (see Eq S2).

Vegetation responds to soil moisture stress through decreases in leaf water potential and stomatal conductance (Garnier and Berger, 1987; Panek and Goldstein, 2001). The effect of soil water on carbon assimilation (i.e. biochemical limitation) is implemented in SIBCASA as (Sellers et al., 1996):

$$V_m = V_{max} f_T(T_c) \beta \qquad \text{(Eq S7)}$$

where V_m represents the leaf-scale maximum catalytic capacity of Rubisco, V_{max0} represents the leaf-scale maximum catalytic capacity of Rubisco at the top of the canopy, and $f_T(T_c)$ represents a scaling parameter function that uses canopy temperature T_c and the temperature response exponent Q_{10}. In addition, SIBCASA applies soil moisture stress to mesophyll conductance ($g_m = 1/r_m$) which is another source for isotope variability in plants (Seibt et al., 2008). In SIBCASA g_m is calculated by the following equation:

$$g_m = 4000 \cdot V_{max0} \cdot \Pi \cdot \beta \qquad \text{(Eq S8)}$$

where factor Π integrates the photosynthetic rate over the entire canopy, and the value 4000 is a chosen constant (Suits et al., 2005). The soil water stress function (β) can thus induce variability in both V_m and g_m.

In eq S7 and S8, β is a function of the Plant Available Water fraction (f_{PAW}) and a shape parameter W_s:

$$\beta = \frac{(1 + W_s) \cdot f_{paw}}{W_s + f_{paw}} \qquad \text{(Eq S9)}$$

f_{PAW} is the total column liquid water that is available to the plant (PAW^t) divided by the maximum amount of liquid water (PAW^m) in each layer (n) of the soil (i.e, field capacity minus wilting point):

$$f_{PAW} = \frac{\sum_{n=1}^{nroot} PAW_n^t}{\sum_{n=1}^{nroot} PAW_n^m} \qquad \text{(Eq S10)}$$

W_s is 0.2 for all biome types in SIBCASA (Schaefer et al., 2008). This results in a soil water stress regulation that is rather conservative, and a steep drop-off in β only occurs when f_{PAW} is < 0.2 (not shown).

LPJ-GUESS

LPJ-GUESS (Smith et al. 2001, 2014) is a process-based second-generation dynamic vegetation-ecosystem model (DVM) optimized for regional to global application. Second-generation DVMs explicitly account for the size and age structure properties and temporal dynamics of woody vegetation stands, as well as landscape heterogeneity resulting from different histories of stochastic disturbance, anthropogenic land use and stand development (succession). Vegetation dynamics result from growth and competition for light, space and soil resources (water, nitrogen) among woody plant individuals and an herbaceous understory. Vegetation is represented as plant functional types (PFTs; 12 to the number in this study as only potential natural vegetation is simulated), each of which are defined by their bioclimatic limits, photosynthetic pathway, growth form, phenology, and life history strategy (i.e. shade tolerance) (Ahlström et al. 2015). Photosynthesis, respiration, stomatal conductance, phenology (leaves and fine roots) and soil properties are simulated on a daily time step. The net primary production (NPP) accrued at the end of each simulation year is allocated to leaves, fine roots and, for woody PFTs, sapwood, following a set of prescribed allometric relationships for each PFT, resulting in height, diameter and biomass growth. Population dynamics (establishment and mortality) are represented as stochastic processes, influenced by current resource status, demography and the life-history characteristics of each PFT (Hickler et al., 2004; Wramneby et al., 2008).

Exchange of CO_2 and water vapour by the vegetation canopy is determined by a coupled photosynthesis and stomatal conductance (g_s) sub-model based on the Collatz et al. (1991, 1992) simplification of the Farquhar biochemical model, with upscaling from leaf to canopy level following the strong optimality approach of Haxeltine and Prentice (1996a, b). In this model, photosynthesis, net of photorespiration, is the smaller of an electron-transport-limited and a carboxylation-limited rate (Collatz et al., 1991), and is affected by incoming photosynthetically active radiation (PAR), temperature, intercellular [CO_2] and carboxylation capacity, V_{max}. The latter is determined prognostically based on the assumption (Haxeltine

and Prentice, 1996a) that plants allocate N (for investment in the enzyme rubisco that determines Vmax) throughout the canopy in a manner that maximizes net CO_2 assimilation at the canopy level. g_s influences water vapour loss (transpiration) from the canopy and intercellular CO_2, thereby coupling C and H_2O cycling by plants and ecosystems. Aggregate g_s at the canopy scale (g_c) is determined by jointly solving the biochemically based expression for photosynthesis and an alternative expression that relates photosynthesis to gc through the diffusion gradient for CO_2 implied by the ratio of intercellular to external CO_2 (C_i/C_a) (Haxeltine and Prentice, 1996b). Under water-stressed conditions a numerical iteration procedure is used to find the level of C_i/C_a which satisfies simultaneously a canopy-conductance based and light-based formulation of photosynthesis (Haxeltine and Prentice,1996b). Available water for plant uptake is independent of water content (to wilting point) but with fractional uptake from different soil layers according to prescribed PFT root distribution and a maximum transpiration rate. Evapotranspiration (ET) encompasses transpiration by plant canopies, evaporation from exposed soil surfaces and evaporation of water intercepted by plant canopies during precipitation events. Canopy transpiration under demand-limited conditions is related to g_s based on an empirical boundary layer parameterisation (Huntingford and Monteith, 1998) that expresses large-scale ET as a hyperbolic dependency on surface resistance (the inverse of g_s), thus avoiding the need for humidity as a driving variable for the model. Under supply-limited conditions ET is determined as a proportion of a maximum rate scaled by root zone water uptake (Haxeltine and Prentice, 1996b; Sitch et al., 2003). Soil evaporation and canopy interception are modeled as described in Gerten et al. (2004).

Plants are subject to maintenance and growth respiration, which are deducted from gross photosynthesis to derive NPP. Leaf respiration scales linearly with V_{max} (Haxeltine and Prentice, 1996a). For the remaining living tissue compartments, i.e. fine roots and sapwood, maintenance respiration depends on N content and follows a modified Arrhenius-dependency on temperature (Lloyd and Taylor, 1994). Growth respiration is one-third of NPP (Ryan 1991).

We made a custom simulation for this project using the latest released version of LPJ-GUESS (4.0; Olin et al. 2015). We used a standard 500 year spin-up (soil 40 000 years) with looped de-trended 1901-1930 climate. Then we ran the historical simulation period 1901 to 2015. CRU-NCEP v7 climate forcing was used for all variables except precipitation (some inconsistencies in the dataset) which instead comes from CRU TS v3.23. The LPJ-GUESS standard resolution is 0.5*0.5 degrees.

LPJ-C13

The isotope enabled version of the Lund-Potsdam-Jena dynamic global vegetation model, LPJ-C13, shares the process formulation of plant physiology and ecosystem biogeochemistry with LPJ-GUESS. However, in contrast to the more detailed scheme that distinguishes woody plant type individuals (cohorts) and represents patch-scale heterogeneity in LPJ-GUESS, LPJ-C13 employs an area-based representation of vegetation structure and dynamics for mean individual plant types. Therefore LPJ-GUESS explicitly models resource competition (light and water) and subsequent growth between woody plant type individuals on a number of replicate patches, while LPJ-C13 simulates competition and growth for mean individuals scaled up to the gridcell level and hence leading to a different drought response. LPJ-C13 models soil moisture as described by Gerten et al. (2004) and Sitch et al. (2003). In brief, plant water stress β is calculated for each Plant Functional Type (PFT) as the minimum between one and the ration of the daily evapotranspiration that can by supplied to the atmosphere by the plant/soil hydrological system, E_{supply}, and the atmospheric demand, E_{demand}:

$$\beta = \min\left[1, \ \frac{E_{supply}}{E_{demand}}\right]. \qquad\qquad \text{(Eq S11)}$$

E_{supply} is determined by the product of plant root-weighted soil moisture (taking into account the PFT-specific rooting depth) and a maximum transpiration rate. E_{demand} is based on Monteith's empirical relationship between evaporation efficiency and surface conductance (Monteith, 1995).

This particular isotope enabled LPJ-C13 model version includes a prognostic calculation of the isotopic discrimination of 13C at the leaf level during the photosynthetic uptake of CO_2 (Scholze et al., 2003, 2008). The isotopic discrimination calculation follows the approach of Lloyd and Farquhar (1994) and is determined by the actual inter-cellular-to-atmospheric CO_2 concentration (C_i/C_a) ratio, which is explicitly simulated by LPJ-C13 through a coupled photosynthesis and water-balance canopy conductance scheme. Furthermore, LPJ-C13 includes a full isotopic terrestrial carbon cycle, i.e. LPJ-C13 calculates the ^{13}C content of all modelled plant and soil carbon pools and fluxes by bookkeeping the ^{13}C signature of the carbon assimilate in its cycling through LPJ-C13's carbon pools.

We used the standard LPJ simulation set up using a 1000 year spin up based on recycling 30 years of climate, followed by a historical simulation over the period 1901-2011 using CRU TS v. 3.25 as climate forcing. Model resolution was 0.5 degrees and the simulations were forced with transient atmospheric CO_2 and $\delta^{13}C$ (based on ice core, firn and atmospheric measurements).

CLM-C13 (CLM4.5)

The Community Land Model version 4.5 (CLM4.5, Oleson et al., 2013) simulates soil moisture stress using a β_t factor defined as

$$\beta_t = \sum_i w_i r_i, \tag{Eq S12}$$

where r_i is the root fraction at soil layer i and w_i is a corresponding plant wilting factor. Root fraction is defined as:

$$r_i = 0.5\left(e^{-r_a z_{h,i-1}} + e^{-r_b z_{h,i-1}}\right) - 0.5\alpha\left(e^{-r_a z_{h,i}} + e^{-r_b z_{h,i}}\right), \tag{Eq S13}$$

where $z_{h,i}$ (m) is the depth from the soil surface to the interface between layers i and $i+1$ ($z_{h,0} = 0$ corresponds to the soil surface), r_a and r_b are root distribution parameters (m^{-1}, defined for each plant functional type), $\alpha = 1$ for $1 \leq i < N$, and $\alpha = 0$ for $i = N$ (N is the number of soil layers). The plant wilting factor is defined as:

$$w_i = \begin{cases} \dfrac{\Psi_c - \Psi_i}{\Psi_c - \Psi_o}\left[\dfrac{\theta_{sat,i} - \theta_{ice,i}}{\theta_{sat,i}}\right] \leq 1 & \text{for } T_i > T_f - 2 \text{ and } \theta_{liq,i} > 0 \\ 0 & \text{for } T_i \leq T_f - 2 \text{ or } \theta_{liq,i} = 0 \end{cases}, \tag{Eq S14}$$

where Ψ_i is the soil water matric potential, Ψ_c and Ψ_o are the soil water potential when stomata are fully closed or fully open, respectively (plant functional type parameters), $\theta_{sat,i}$ is the saturated volumetric water content, $\theta_{ice,i}$ is the volumetric ice content, $\theta_{liq,i}$ is the volumetric liquid water content, T_i is the soil layer temperature, and $T_f = 273.15$ K is the freezing temperature of water. The sum in Eq. (S12) is defined over the entire soil column, resulting in β_t values from 0 (maximum soil moisture stress) to 1 (no soil moisture stress).

In CLM4.5, β_t is used to downscale the maximum rate of carboxylation (i.e., $\beta_t V_{cmax}$) and also leaf respiration (i.e., $\beta_t R_d$), so net leaf photosynthesis (A_n) is directly impacted by soil moisture stress. Leaf stomatal conductance is also impacted by β_t. As in SIBCASA, CLM4.5 simulates g_s based on the Ball-Berry model (cf. Eq. S6):

$$g_s = m\frac{A_n}{C_s}h_s P + b\beta_t. \tag{Eq S15}$$

Note, however, that in CLM4.5's implementation of the Ball-Berry model, β_t is used to downscale b, directly impacting g_s. The soil moisture stress factor β_t also indirectly impacts g_s through the A_n term, as discussed above. In CLM4.5, the parameters m and b are defined as 9 (4) and 10 (40) mmol m^{-2} leaf s^{-1} for C$_3$ (C$_4$) plants, respectively. CLM4.5 accounts for atmospheric water stress in the calculation of g$_s$. Note

that the first term on the R.H.S. of Eq. S15 is downscaled by the relative humidity at the leaf surface (h_s). For further information, the reader is referred to the CLM4.5 documentation (Oleson et al., 2013).

For this study we run a CLM4.5-CN configuration with inactive fire, ~0.9ox1.25o surface maps, and CRUNCEP atmospheric forcing (included in the Community Earth System Model, version 1.2 (CESM1.2) – see http://www.cesm.ucar.edu/models/cesm1.2/clm/clm_forcingdata_esg.html for further information).

We spun-up the model under pre-industrial conditions, using land cover, atmospheric CO_2 and $\delta 13CO_2$, and aerosol and nitrogen deposition values for year 1850 (we fixed the atmospheric CO_2 and $\delta 13CO_2$ at 285 ppmv and −6.6 ‰, respectively, and used the land cover and aerosol and nitrogen deposition datasets included in CESM1.2). We conducted an initial 600-years spin-up in accelerated decomposition mode, followed by a final 200-years spin-up in standard mode. CRU-NCEP data from 1901 to 1950 were continuously cycled during the spin-up.

After model spin-up, we conducted a transient run (1850–2010) using transient land cover, atmospheric CO_2 and $\delta 13CO_2$, and aerosol and nitrogen deposition. We used monthly atmospheric CO_2 and $\delta 13CO_2$ data, zonally resolved, to drive the model, with the same forcing as van der Velde et al. (2014). For land cover and aerosol and nitrogen deposition we used the RCP8.5 datasets in CESM1.2, which include historical data up to 2005, followed by RCP8.5 scenario data. We used CRU-NCEP data from 1901 to 1951 to drive the model from 1850 to 1900, then CRU-NCEP data from 1901 to 2010 to drive the model from 1901 to 2010.

JULES (v4.4-GL6-modified)

JULES (Clarks et al. 2011; Best et al. 2011) applies soil water stress to V_{cmax} and J_{max}:

$$V_{cmax} = V_{cmax,0} \cdot \beta \qquad \text{(Eq S16)}$$

$$J_{max} = J_{max,0} \cdot \beta \qquad \text{(Eq S17)}$$

where $V_{cmax,0}$ and $J_{max,0}$ are the potential (i.e. unstressed) V_{cmax} and J_{max} values, respectively, and β is the dimensionless moisture stress factor, which is related to the mean soil moisture concentration in the root zone, computed as a function of volumetric soil water content (θ m^3 m^{-3}) and varying linearly between field capacity (θ_{FC}) and wilting point (θ_{WP}):

$$\beta = \begin{cases} 1 & \theta \geq \theta_{FC} \\ \left[\frac{\theta - \theta_{WP}}{\theta_{FC} - \theta_{WP}} \right] & \theta_{WP} < \theta < \theta_{FC} \\ 0 & \theta \leq \theta_{WP} \end{cases}$$

This formulation corresponds to that used in experiment C2 of Egea et al (2011).

The version of JULES used is 4.4, with the scientific formulation (GL6) described in the paper by Walters et al. (2017). Spinup is performed, starting with a previously existing climatology as initial condition, by iterative repeating the first year of simulation (1979), also forced by 0.5deg WFDEI meteo data, until the solutions converge on two in-soil prognostic variables, at all points in the Northern Hemisphere, following these criteria: (1) for soil moisture: to within 1% of content, (2) for soil temperature: to within 0.1K. We attempt this for a maximum of 35 iterations. For the experiments described in this paper, the GL6 formulation was modified to:

- use Brooks-Corey (BC) (1964) soil hydraulic equations, instead of the Van Genuchten (VG) formulation, which was until recently set as standard in JULES

- use the SoilGrids global soils map created by Carsten Montzka (see Montzka et al. 2017), which were processed using the ROSETTA software described in Schaap et al. (2001) to produce physical parameters for the Brooks and Corey (1964) parameterization.

The main reason for the decision to switch from VG to BC was the fact that the standard set of global parameters supplied via the JULES ancillary files is derived from pedotransfer functions (Cosby et al., 1984) that are designed to be used with BC, not with VG. The BC parameters can be transformed to VG, but this will lead to inaccuracies. Note that the choice of soil hydraulic model is not mentioned in Table S4, because this is somewhat beyond the scope of this paper. However, Verhoef and Egea (2014) showed that the choice of soil hydraulic model in land surface and related global climate models, and the selected parameter values, is important, as it can exert a significant influence on β. JULES has been setup exactly as we intend our CMIP6 (HighResMIP) submission to be, once coupled into the GCM for phase 2 of PRIMAVERA experiments.

ORCHIDEE-MICT (v8.4.1)

ORCHIDEE-MICT (Guimberteau et al., 2017) is a branch of the ORCHIDEE land surface model (Krinner et al., 2005) with additional processes that are important for the high latitudes, including a soil freezing scheme describing its effect on water infiltration and phase change-induced heat fluxes in the soil column (Gouttevin et al., 2012); a multi-layer snow scheme which improves the representation of snow thermal conductivity and soil temperature (Wang et al., 2013); the impact of soil organic matter on soil thermal and hydraulic properties that increases thermal insulation and available water capacity of the soil (Guimberteau

et al., 2017); and a vertically resolved soil carbon module considering cryoturbation in permafrost soils (Koven et al., 2009). ORCHIDEE simulates photosynthesis at half-hourly time-step, and simulates phenology and the allocation of GPP assimilates to autotrophic respiration and plant biomass pools at daily time-step.

The leaf-level photosynthesis is simulated using the Farquhar model, coupled with the diffusional conductance of three components (boundary-layer, stomatal and mesophyll) using the formulations proposed by Yin and Struik (2009). The stomatal conductance is calculated as:

$$g_s = g_0 + \frac{A_g + N_d}{C_i - C_i^*} f_{VPD}$$

$$f_{VPD} = (\frac{1}{a - b \cdot VPD} - 1)^{-1} \tag{Eq S19}$$

where R_d is the dark respiration in daytime; g_0 is the residual stomatal conductance if the irradiance approaches zero; C_{i*} is the C_i-based CO_2 compensation point in the absence of R_d; f_{vpd} is the effect of leaf-to-air vapor pressure deficit (VPD). The coefficients a and b follow Yin and Struik (2009).

The soil moisture stress factor (β) is calculated based on the relative moisture content at each soil layer (ORCHIDEE has 11 layers for hydrology down to 2 meters), defined as:

$$\beta_i = \frac{\theta_i - \theta_{wp}}{\theta_{wp} + p(\theta_{fc} - \theta_{wp})} \tag{Eq S20}$$

$$\beta = \sum_{i=1}^{11} \beta_i \cdot w_i \tag{Eq S21}$$

Where β_i is relative moisture content at each soil layer i, bounded between 0 and 1; θ_{wp} and θ_{fc} are soil moisture at wilting point and field capacity respectively; p represents the threshold of relative soil moisture in each layer above which photosynthesis rate parameters and stomatal conductance parameters are not limited by soil moisture, and is set at 0.8; w_i is the weighting factor for each layer, calculated dynamically to optimize plant water use:

$$w_i = \frac{\beta_i}{\sum_{i=1}^{11} \beta_i} \tag{Eq S22}$$

If layer i is below modeled active layer thickness (namely, this layer is permanently frozen), w_i is set to zero, and the remaining w are re-normalized to one.

Soil moisture is redistributed in the column by solving the Richards equation for vertical unsaturated flow under the effect of root uptake. Note that ORCHIDEE considers different soil types from the USDA texture map with 12 different soil texture types associated with different hydraulic parameters controlling the saturation conductivity and water diffusivity, the field capacity and the wilting point. In the same grid cell, the dominant USDA texture map is used at the working model spatial resolution. Each grid cell contains three different soil tiles with all herbaceous vegetation, all tree vegetation and bare soils respectively, and these soil tiles have a separate soil water budget.

In ORCHIDEE-MICT, β multiplies V_{max}, J_{max}, g_s, g_m, and R_d, to downscale them under soil moisture stress.

The model run used here is a custom simulation for this study. The model version (Guimberteau et al. 2018) is the same as the one used for TRENDY-v6 (Le Quéré et al. 2018) except for an updated algorithm for the soil carbon cryoturbation. Spin-up of the model used the climate forcing from CRU-NCEP v8, and covered 200 years of the full model + 20,000 years of the soil carbon sub-model, forced by looped 1901-1920 climate, and the 1860 land cover map. The analyzed simulation period was 1860-2011 and this period was run with changing climate, changing atmospheric CO_2, and changing land use. The spatial resolution of our simulation was 2 by 2 degrees.

S7: The NH land Δ and NEE anomalies in six land-surface models

With the models as described above, we derived the statistics as visualized in Fig 3 of the main text. Values displayed in Fig 3 are provided here in Table S5.

Table S5: Statistics of the Δ-NEE relationships across six land-surface models for the carbon cycle, compared to the inversely derived values. We based this comparison on TransCom region definitions (NH land = TC1 + TC2 + TC7 + TC8 + TC10), Slopes that are significantly different from 0 are highlighted with single ($p<0.05$, N=9) or double ($p<0.01$, N=9) asterisks. Note that the B1 simulation is only one of four inversions from Table S2 that were averaged into the results for Fig 1, and the statistics are therefore not exactly the same. In Fig 3 of the main text, radii R_Δ and R_{NEE} correspond to row 4 and 5 of this table.

|	Inverse (B1)	SIBCASA	CLM4.5	LPJ-GUESS	LPJ-13C	JULES	ORCHIDEE
	C3+C4 AREAS, NH Temperate+Boreal						
correlation [-]	-0.79	0.14	0.37	-0.61	0.05	-0.77	-0.08
slope [‰/(PgC/yr)]	-0.29	0.01	0.06	-0.04	0.01	-0.12	-0.02
p-value [-]	0.003**	0.650	0.270	0.05*	0.887	0.006**	0.806
IAV in Δ [‰] (R_Δ)	0.18	0.02	0.05	0.06	0.13	0.04	0.03
IAV in NEE [PgC/yr] (R_{NEE})	0.49	0.29	0.34	0.94	0.82	0.22	0.15
	Europe 2003 annual mean anomalies						
Delta [‰]	-0.64	-0.26	0.04	-0.67	-1.80	-0.21	-0.29
iWUE [%]	12.80	5.35	-1.04	19.17	22.40	10.10	11.24
NEE [TgC/yr]	79.70	-98.90	301.80	623.00	283.30	135.40	79.44
GPP [TgC/yr]	N/A	-153.79	-469.05	-735.7	-523.7	-613.5	-318.90
TER [TgC/yr]	N/A	-252.69	-167.26	-100.04	-246.7	-478.1	-221.10

The last two rows correspond to the simulated GPP and TER anomalies of these models for 2003, a number which is not available from the inverse estimate. We provide Fig S9 to illustrate the large spread in the drought impact on GPP and TER across the models, which shows these anomalies along with two lines that denote an 79.7 TgC/yr difference between TER and GPP as suggested by the inverse estimate. The size of
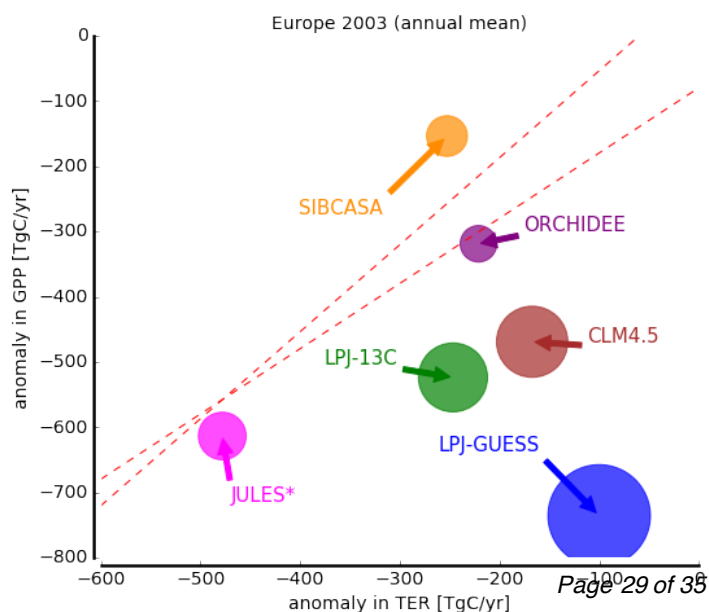
Figure S9: The 2003 drought anomaly in six terrestrial biosphere models. Shown are the annual mean anomalies in GPP (y-axis) and TER (x-axis), with symbol sizes relative to the NEE anomaly of each model. Negative anomalies point to a reduction of GPP and TER during the drought. The red lines show two combinations of GPP and TER that add up to the inversely derived NEE anomaly of 79.9 TgC/yr. Note that uncertainty on this total NEE anomaly was not estimated, but can be as large as 100 TgC/yr.

the colored circles is proportional to the NEE anomaly for each model. We note that these differences come on top of large differences in the long-term mean GPP, TER, and NEE between the models: the NH net carbon uptake ranges from 0.25 PgC/yr (SIBCASA) to 12.3 PgC/yr (JULES), with other models falling in the expected range of 2.0-3.0 PgC/yr. The large imbalance in the JULES simulations is due to the respiration from its single soil carbon pool, which was not explicitly tuned to balance GPP in this simulation. Anomalies in GPP, TER, NEE, and Ci/Ca should nevertheless be valid, and models such as JULES and ORCHIDEE with an NEE anomaly closer to the observed values are more likely to simulate a correct atmospheric CO_2 anomaly during droughts.

In addition, we provide in Fig S10 a visual comparison of the derived iWUE anomalies over Europe during 2003, compared also to the eddy-covariance derived changes shown in Table S2. Fig S11 shows the NEE and Δ anomalies for each model during 2003 and 2010 across the NH.
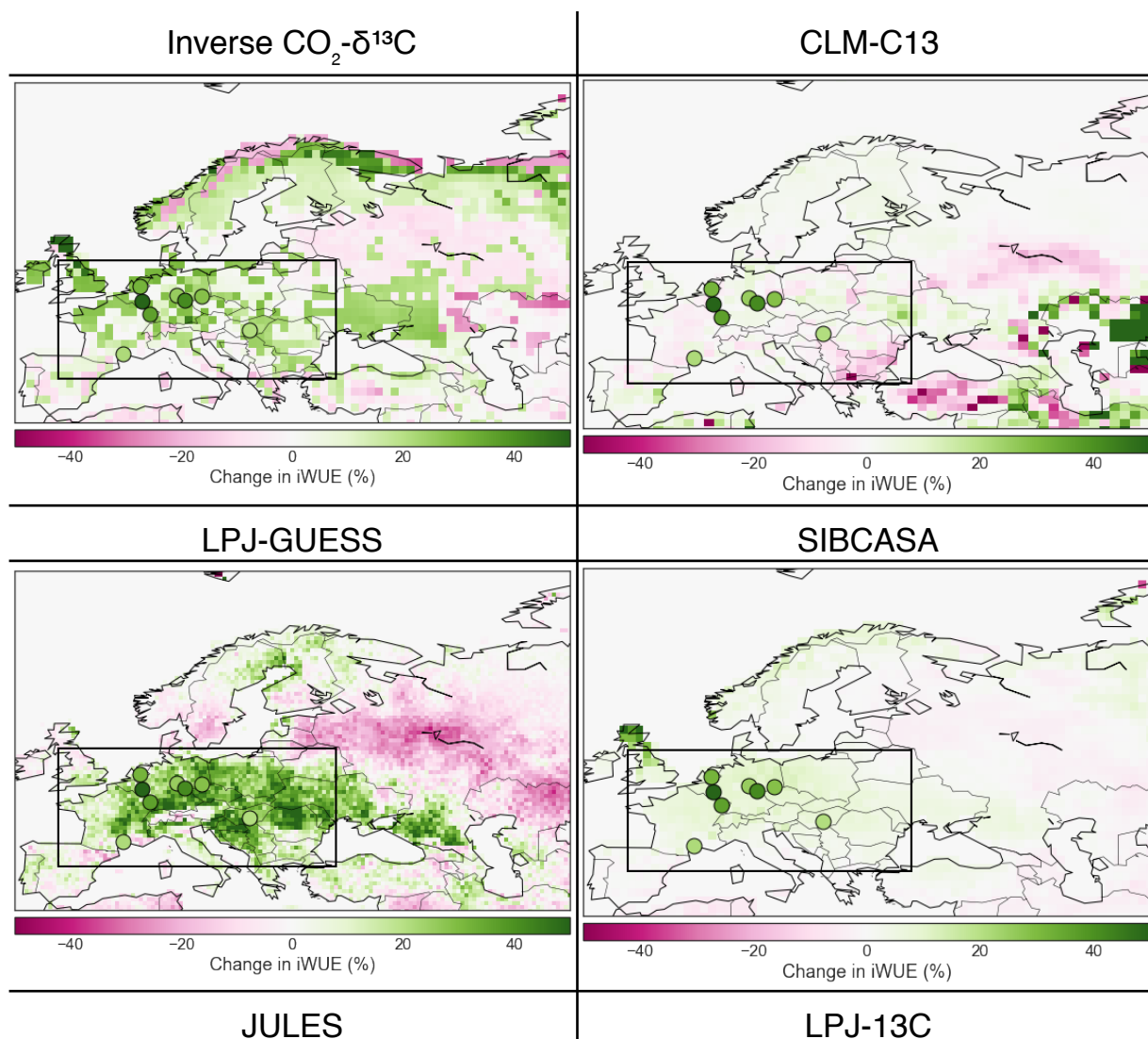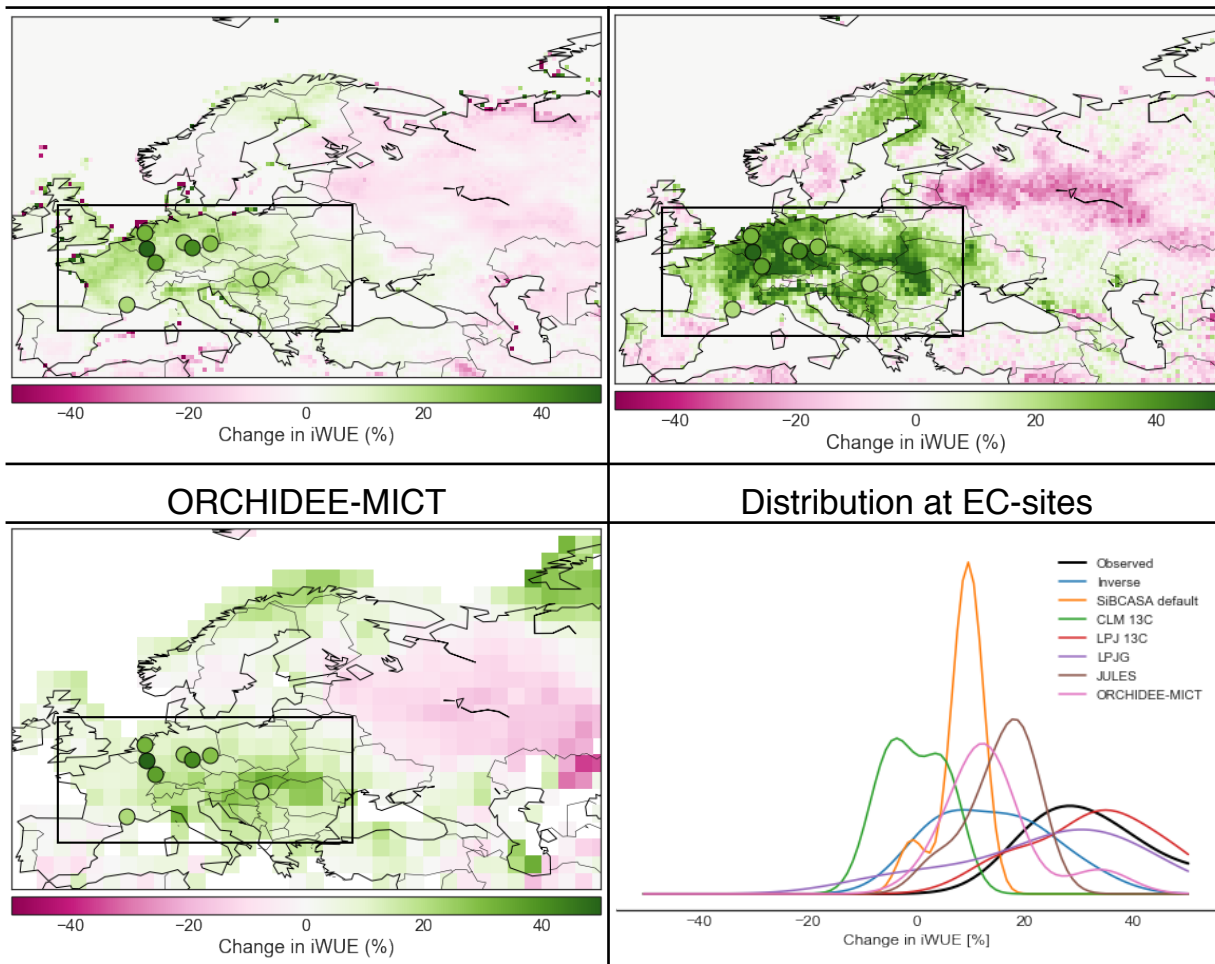
Figure S10: Relative change in iWUE (%) over Europe and western Russia during the 2003 drought. The values represent GPP-weighted means for the year 2003 compared to the 2001-2011 average of each model. Colored dots are changes in inherent water-use efficiency derived from eddy-covariance data. The bottom-right distributions show the changes over these N=8 sites as subsampled in the model domain. The box refers to the averaging domain used in deriving the anomalies shown in Table S4
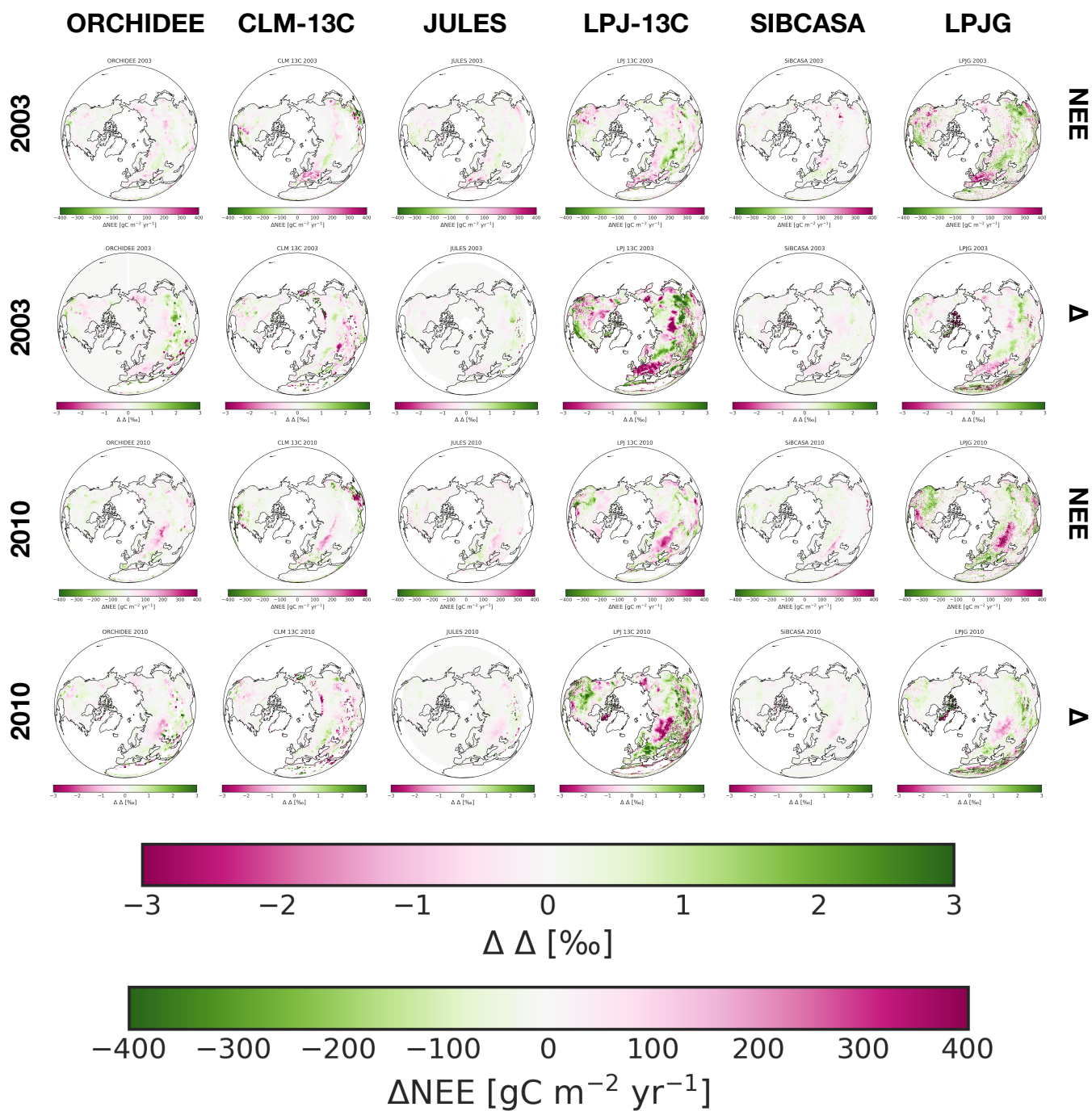
Figure S11: Anomalies of Δ and NEE for the suite of six terrestrial biosphere models used during the summer of 2003 and 2010. Colorbars are the same for each panel and enlarged for clarity.

References

Ahlström, A., et al., The dominant role of semi-arid ecosystems in the trend and variability of the land CO_2 sink. Science, 348, 895-899, (2015).

Alden, C. B., et al., Can bottom-up ocean CO_2 fluxes be reconciled with atmospheric ^{13}C observations? Tellus, Ser. B, 62(5), 369–388, doi:10.1111/j.1600-0889.2010.00481.x (2010)

Ball, J. "An Analysis of Stomatal Conductance." Ph.D. Thesis, Stanford University. (1988)

Ballantyne, A. P., et al., Apparent seasonal cycle in isotopic discrimination of carbon in the atmosphere and biosphere due to vapor pressure deficit. Global Biogeochemical Cycles 24, GB3018 (2010).

Ballantyne, A. P., et al., Novel applications of carbon isotopes in atmospheric CO_2: what can atmospheric measurements teach us about processes in the biosphere? Biogeosciences 8, 3093–3106 (2011).

Beer, C., et al., Temporal and among-site variability of inherent water use efficiency at the ecosystem level, Global Biogeochemical Cycles, 23, GB2018, doi:10.1029/2008GB003233. (2009)

Best et al., The Joint UK Land Environment Simulator (JULES), model description – Part 1: Energy and water fluxes. Geosci. Model Dev. 4:677–699, (2011)

Bréda, N. et al., Temperate Forest Trees and Stands under Severe Drought: A Review of Ecophysiological Responses, Adaptation Processes and Long-Term Consequences." Annals of Forest Science 63 (6): 625–44. doi:10.1051/forest:2006042. (2006)

Brooks, R. J. and Corey, A. T. Hydraulic properties of porous media, Colorado State University Fort Collins, CO, USA, Hydrology Papers, 3, 37 pp., (1964).

Brüggemann, N. et al. Carbon allocation and carbon isotope fluxes in the plant-soil-atmosphere continuum: a review. Biogeosciences 8:3457-3489 (2011)

Ciais, P. et al. Europe-wide reduction in primary productivity caused by the heat and drought in 2003. Nature 437, 529–533. (2005)

Ciais, P. et al., Partitioning of ocean and land uptake of CO_2 as inferred by ^{13}C measurements from the NOAA Climate Monitoring and Diagnostics Laboratory Global Air Sampling Network, J. Geophys. Res., 100, 5051–5070, (1995)

Clark et al., The Joint UK Land Environment Simulator (JULES), model description – Part 2: Carbon fluxes and vegetation dynamics. Geosci. Model Dev. 4:701–722. (2011)

Collatz, G. J. et al., Coupled photosynthesis-stomatal conductance model for leaves of C4 plants, Aust. J. Plant Physiol., 19, 519–538, (1992).

Collatz, G. J. et al., Physiological and environmental regulation of stomatal conductance, photosynthesis, and transpiration: a model that includes a laminar boundary layer. Agric. and Forest Meteorol. 54, 107–136 (1991).

Cosby, B.J. et al., A statistical exploration of the relationships of soil moisture characteristics to the physical characteristics of soils, Water Resour. Res., 20, 682-690. (1984)

Egea, G., Verhoef, A. and Vidale, P. L. Towards an improved and more flexible representation of water stress in coupled photosynthesis–stomatal conductance models. Agricultural and Forest Meteorology, 151 (10). pp. 1370-1384. ISSN 0168-1923 doi: 10.1016/j.agrformet.2011.05.019 (2011)

Ekblad, A, and P Hogberg. Natural Abundance of C-13 in CO_2 Respired From Forest Soils Reveals Speed of Link Between Tree Photosynthesis and Root Respiration. Oecologia 127: 305–8, (2001)

Farquhar, G. D., M. H. O'Leary, and J. A. Berry, On the relationship between carbon isotope discrimination and the intercellular carbon dioxide concentration in leaves, Aust. J. Plant. Physiol., 9, 121 – 137. (1982)

Farquhar, G. D., S. von Caemmerer, and J. A. Berry, A biochemical model of photosynthetic CO_2 assimilation in C3 plants. Planta, 149, 78-90, (1980)

Farquhar, G D, and R A Richards. Isotopic Composition of Plant Carbon Correlates with Water-Use Efficiency of Wheat Genotypes. Functional Plant Biology 11 (6). CSIRO PUBLISHING: 539–52. doi:10.1071/pp9840539. (1984)

Gerten, D., et al., Terrestrial vegetation and water balance—hydrological evaluation of a dynamic global vegetation model. Journal of Hydrology, 286, 249-270, doi: 10.1016/j.jhydrol.2003.09.029. (2004).

Graven, H. D. et al., Enhanced seasonal exchange of CO_2 by northern ecosystems since 1960. Science 341, 1085–1089 (2013)

Guimberteau, M. et al., ORCHIDEE-MICT (v8.4.1), a land surface model for the high latitudes: model description and validation. Geosci. Model Dev. 11, 121–163 (2018).

Gurney, K. R., et al., Towards robust regional estimates of CO_2 sources and sinks using atmospheric transport models, Nature, 415, 626-630, doi:10.1038/415626a, (2002)

Haxeltine, A. and Prentice, I. C. A general model for the light-use efficiency of primary production, Funct. Ecol., 10, 551–561, (1996a).

Haxeltine, A. and Prentice, I. C. BIOME3: An equilibrium terrestrial biosphere model based on ecophysiological constraints, resource availability, and competition among plant functional types, Global Biogeochem. Cy., 10, 693–709, (1996b).

Hengl T, et al. SoilGrids250m: Global gridded soil information based on machine learning. PLoS ONE 12(2): e0169748. doi:10.1371/journal.pone.0169748 (2017)

Hickler, T. et al., CO_2 fertilization in temperate forest FACE experiments not representative of boreal and tropical forests, Glob. Change Biol., 14, 1531–1542, (2008).

Huntingford, C. and Monteith, J. L. The behaviour of a mixed-layer model of the convective boundary layer coupled to a big leaf model of surface energy partitioning, Bound.-Lay. Meteorol., 88, 87–101, (1998).

Jacobs, C M J. "Direct Impact of Atmospheric CO2 Enrichment on Regional Transpiration." PhD thesis, Wageningen University (1994)

Katul, G., D. S. Ellsworth, and C.-T. Lai, Modelling assimilation and intercellular CO_2 from measured conductance: a synthesis of approaches, Plant, Cell Environ., 23, 1313–1328, (2010)

Keeling, C. D., The Suess effect: 13Carbon-14Carbon interrelations. Environment International, 2(4-6):229–300. (1979).

Krol, M., et al., The two-way nested global chemistry-transport zoom model TM5: algorithm and applications, Atmos. Chem. Phys., 5, 417-432, doi:10.5194/acp-5-417-2005, (2005).

Kurbatova, J., C. et al., Modeling carbon dynamics in two adjacent spruce forests with different soil conditions in Russia, Biogeosciences, 5, 969-980, doi:10.5194/bg-5-969-2008, (2008)

Kurbatova, J., F. et al., Partitioning of ecosystem respiration in a paludified shallow-peat spruce forest in the southern taiga of European Russia. Environ. Res. Lett. 8, 045028, (2013).

Leuning, R., A critical appraisal of a combined stomatal photosynthesis model for C3 plants, Plant, Cell Environ., 18, 339–355, (1995).

Leuning, R., Kelliher, F. & Pury, D. Leaf nitrogen, photosynthesis, conductance and transpiration: scaling from leaves to canopies. Plant (1995).

Lloyd, J. and Taylor, J. A. On the temperature dependence of soil respiration, Funct. Ecol., 8, 315–323, (1994).

Lloyd, J., and G. Farquhar,. 13C discrimination during CO_2 assimilation by the terrestrial biosphere, Oecologia, 99, 201–215. (1994)

Medlyn, B. et al, How Do Leaf and Ecosystem Measures of Water-Use Efficiency Compare?. New Phytologist 216 (3): 758–70. doi:10.1111/nph.14626. (2017).

Monteith, J.L.. Accommodation between transpiring vegetation and the convective boundary layer. J. Hydrol. 166, 251–263. (1995)

Montzka, C., et al., A global data set of soil hydraulic properties and sub-grid variability of soil water retention and hydraulic conductivity curves. Earth System Science Data, 9 (2). pp. 529-543. ISSN 1866-3516 doi: 10.5194/essd-9-529-2017 , (2017).

Oleson, K. W. et al., Technical description of version 4.5 of the Community Land Model (CLM), NCAR Earth System Laboratory – Climate and Global Dynamics Division, Boulder, Colorado, USA, Tech. Rep. TN-503+STR, (2013).

Olin, S., Lindeskog, M., Pugh, T., Schurgers, G., Mischurow, M., Wårlind, D., Zaehle, S., Stocker, B., Smith, B. and Arneth, A. 2015. Soil carbon management in large-scale Earth system modelling: implications for crop yields and nitrogen leaching. Earth System Dynamics, 6, 745-768. doi:10.5194/esd-6-745-2015

Olson, J. S., J. A. Watts, and L. J. Allison, Major world ecosystem complexes ranked by carbon in live vegetation. Carbon Dioxide Information Center, Oak Ridge National Laboratory, Oak Ridge TN. (1985)

Peters, W., et al., Seven years of recent European net terrestrial carbon dioxide exchange constrained by atmospheric observations. Global Change Biology, 16, 1317–1337, doi: 10.1111/j. 1365-2486.2009.02078.x. (2010).

Peters, W., et al., An ensemble data assimilation system to estimate CO_2 surface fluxes from atmospheric trace gas observations, J. Geophys. Res., 110, D24304, doi:10.1029/2005JD006157, (2005)

Raczka, Brett, Henrique F Duarte, Charles D Koven, Daniel Ricciuto, Peter E Thornton, John C Lin, and DAVID R BOWLING. 2016. "An Observational Constraint on Stomatal Function in Forests: Evaluating Coupled Carbon and Water Vapor Exchange with Carbon Isotopes in the Community Land Model (CLM4.5)." Biogeosciences 13 (18). Copernicus GmbH: 5183–5204. doi:10.5194/bg-13-5183-2016.

Ryan, M. G. Effects of climate change on plant respiration, Ecol. Appl., 1, 157–167, (1991).

Schaap, M.G., F.J. Leij, and M. Th. van Genuchten,. Rosetta: a computer program for estimating soil hydraulic parameters with hierarchical pedotransfer functions. Journal of Hydrology, 251:163-176, (2001)

Schaefer, K. et al., The combined Simple Biosphere/Carnegie–Ames–Stanford Approach (SIBCASA) model, J. Geophys. Res., 113, G03034, doi:10.1029/2007JG000603, (2008).

Scholze, M. et al., Climate and interannual variability of the atmosphere-biosphere 13CO$_2$ flux, Geophys. Res. Lett., 30, 1097, doi:10.1029/2002GL015631, (2003)

Seibt, U. et al., Carbon isotopes and water use efficiency: sense and sensitivity, Oecologia, 155, 441-454, (2008)

Sellers, P. J. et al., A Revised Land Surface Parameterization (SiB2) for Atmospheric GCMS, Part I: Model Formulation, J. Climate, 9, 676–705, (1996).

Sitch, S. et al., Evaluation of ecosystem dynamics, plant geography and terrestrial carbon cycling in the LPJ Dynamic Global Vegetation Model, Glob. Change Biol., 9, 161–185, (2003).

Sitch, S. et al., Evaluation of ecosystem dynamics, plant geography and terrestrial carbon cycling in the LPJ dynamic global vegetation model. Glob. Change Biol. 9, 161–185 (2003).

Smith, B., Prentice, I. C., and Sykes, M. T., Representation of vegetation dynamics in the modelling of terrestrial ecosystems: comparing two contrasting approaches within European climate space, Glob. Ecol. Biogeogr., 10, 621–637, (2001).

Smith, B., et al., Implications of incorporating N cycling and N limitations on primary production in an individual-based dynamic vegetation model, Biogeosciences, 11, 2027–2054, (2014).

Suess, H E, and H Wänke. "Radiocarbon Content and Terrestrial Age of Twelve Stony Meteorites and One Iron Meteorite." Geochimica Et Cosmochimica Acta (4). Pergamon: 475–80. doi: 10.1016/0016-7037(62)90092-3, (1962)

Suits, N. S. et al., Simulation of carbon isotope discrimination of the terrestrial biosphere, Global Biogeochem. Cycles, 19, GB1017, doi:10.1029/2003GB002141, (2005).

Takahashi, T., et al., Climatological mean and decadal change in surface ocean pCO(2), and net sea-air CO$_2$ flux over the global oceans, Deep Sea Res. Part II, 56(8–10), 554–577, doi:10.1016/ j.dsr2.2008.12.009, (2009)

Tans, P. P., J. A. Berry, and R. F. Keeling, Oceanic ^{13}C/^{12}C observations: A new window on ocean CO$_2$ uptake, Global Biogeochem. Cycles, 7(2), 353–368, doi:10.1029/93GB00053, (1993)

Tarantola, A., Inverse problem theory and methods for model parameter estimation, Society for Industrial and Applied Mathematics, Philadelphia, PA. (2005)

Van der Velde, I. R. et al., Terrestrial cycling of ^{13}CO$_2$ by photosynthesis, respiration, and biomass burning in SIBCASA, Biogeosciences, 11, 6553-6571, doi:10.5194/bg-11-6553-2014, (2014).

Van der Velde, I. R. et al., Biosphere model simulations of interannual variability in terrestrial 13C/12C exchange, Global Biogeochem. Cycles, 27, 637–649, doi:10.1002/gbc.20048, (2013).

van der Velde, I. R. et al., The CarbonTracker Data Assimilation System for CO$_2$ and δ^{13}C (CTDAS-C13 v1.0): retrieving information on land-atmosphere exchange processes, Geoscientific Model Development, Accepted, discussion paper at doi:10.5194/gmd-2017-84. (2017)

Verhoef, A. and Egea, G., Modeling plant transpiration under limited soil water: comparison of different plant and soil hydraulic parameterizations and preliminary implications for their use in Land Surface Models. Agriculture and Forest Meteorology, 191, 22–32, (2014).

Walters, D. N., et al., The Met office unified model global atmosphere 6.0/6.1 and JULES global land 6.0/6.1 configurations. Geosci. Model Dev. 10(4), 1–52. DOI: 10.5194/gmd-2016-194, (2017).

Wramneby, A. et al., Parameter uncertainties in the modelling of vegetation dynamics – effects on tree community structure and ecosystem functioning in European forest biomes, Ecol. Model., 216, 277–290, (2008).

Yin, X, and P C Struik. 2009. "C3 and C4 Photosynthesis Models: an Overview From the Perspective of Crop Modelling." Recent Advances in Crop Growth Modelling 57 (1): 27–38.

Zhang, J., Quay, P. D., and Wilbur, D. O, Carbon isotope fractionation during gas-water exchange and dissolution of CO$_2$, Geochim. Cosmochim. Acta 59, 107–114, (1995).